A NUMERICAL INVESTIGATION OF HELICOPTER FLOW FIELDS INCLUDING THERMAL EFFECTS OF EXHAUST HOT GASES

A THESIS SUBMITTED TO
THE GRADUATE SCHOOL OF NATURAL AND APPLIED SCIENCES
OF
MIDDLE EAST TECHNICAL UNIVERSITY

BY

ZEYNEP ECE GÜRSOY

IN PARTIAL FULFILLMENT OF THE REQUIREMENTS
FOR
THE DEGREE OF MASTER OF SCIENCE
IN
AEROSPACE ENGINEERING

SEPTEMBER 2009

Approval of the thesis:

A NUMERICAL INVESTIGATION OF HELICOPTER FLOW FIELDS INCLUDING THERMAL EFFECTS OF EXHAUST HOT GASES

submitted by **ZEYNEP ECE GÜRSOY** in partial fulfillment of the requirements for the degree of **Master of Science in Aerospace Engineering Department, Middle East Technical University** by,

Prof. Dr. Canan Özgen _____
Dean, Graduate School of **Natural and Applied Sciences**

Prof. Dr. İ. Hakkı Tuncer _____
Head of Department, **Aerospace Engineering**

Prof. Dr. Yusuf Özyörük _____
Supervisor, **Aerospace Engineering Dept., METU**

Examining Committee Members:

Prof. Dr. Nafiz Alemdaroğlu _____
Aerospace Engineering Dept., METU

Prof. Dr. Yusuf Özyörük _____
Aerospace Engineering Dept., METU

Assoc. Prof. Dr. Serkan Özgen _____
Aerospace Engineering Dept., METU

Dr. Dilek Funda Kurtuluş _____
Aerospace Engineering Dept., METU

H.Özgür Demir, M.Sc. _____
Senior Expert Engineer, ASELSAN

Date: 11.09.2009

I hereby declare that all information in this document has been obtained and presented in accordance with academic rules and ethical conduct. I also declare that, as required by these rules and conduct, I have fully cited and referenced all material and results that are not original to this work.

Name, Surname: Zeynep Ece Gürsoy

Signature:

ABSTRACT

A NUMERICAL INVESTIGATION OF HELICOPTER FLOW FIELDS
INCLUDING THERMAL EFFECTS OF EXHAUST HOT GASES

Gürsoy, Zeynep Ece
M. Sc., Department of Aerospace Engineering
Supervisor: Prof. Dr. Yusuf Özyörük

September 2009, 86 pages

This thesis investigates the flow field of a twin-engine, medium lift utility helicopter numerically. The effects of the exhaust hot gases emerging from the engines are accounted for in the numerical study. The commercial computational fluid dynamics (CFD) software ANSYS Fluent is employed for the computations. While the effects of engines are included in the computations through simple inlet and outlet boundary conditions, the main and tail rotors are simulated by the Virtual Blade Model in a time-averaged fashion. Forward flight at four different advance ratios and hover in ground effect are studied. The temperature distribution around the tail boom is compared to available flight test data. Good agreement with the flight test data is observed.

Keywords: Helicopter, CFD, engine effects, Virtual Blade Model, Fluent.

ÖZ

MOTOR EGZOZ SICAK GAZ ETKİLERİNİ DE İÇEREN HELİKOPTER AKIŞ ALANLARININ SAYISAL OLARAK İNCELENMESİ

Gürsoy, Zeynep Ece
Yüksek Lisans, Havacılık ve Uzay Mühendisliği Bölümü
Tez Yöneticisi: Prof. Dr. Yusuf Özyörük

Eylül 2009, 86 sayfa

Bu tez çift motorlu, orta kapasiteli bir genel maksat helikopterinin akış alanını sayısal olarak incelemektedir. Sayısal çalışmada motorlardan çıkan sıcak gazların etkileri hesaba katılmaktadır. Hesaplamalı çözümlemeler için ticari hesaplamalı akışkanlar dinamiği (HAD) yazılımı ANSYS Fluent kullanılmaktadır. Motorların etkileri hesaplamalara basit sınır koşulları olarak katılırken ana ve kuyruk rotoru benzetimi Sanal Pal Modeli ile zaman-ortalamalı şekilde gerçekleştirilmektedir. Dört ilerleme hızında ileri uçuş ve yer etkisinde askı durumu incelenmektedir. Kuyruk bumu çevresindeki sıcaklık dağılımı eldeki uçuş test verileri ile karşılaştırılmaktadır. Uçuş test verileriyle uyumlu sonuçlar gözlenmektedir.

Anahtar kelimeler: Helikopter, HAD, motor etkileri, Sanal Pal Modeli, Fluent.

To my family

ACKNOWLEDGEMENTS

I would like to express my gratitude to my supervisor Prof. Dr. Yusuf ÖZYÖRÜK for his guidance, advice and encouragement.

I also would like to thank Prof. Dr. Nafiz ALEMDAROĞLU for his guidance, advice and encouragement.

I am indebted to Özgür DEMİR and Vahit ÖZVEREN for their invaluable guidance, support and friendship, Uğur ETİZ, Murat PARLAK and Okan PEKEL for their support and friendship. I also would like to thank Sevinç FAHRI for helping me, in her busiest time, with obtaining some of the data used in this thesis and for her friendship.

I would like to extend my gratitude to ASELSAN Inc. for providing me with the necessary software and hardware.

Finally, I owe my deepest gratitude to my parents Nuray and Ekrem GÜRSOY, my sister Hande GÜRSOY, my aunt, and my friends – Aybeniz YİĞİT in particular – for their love, patience, support, understanding and encouragement.

TABLE OF CONTENTS

LIST OF TABLES

TABLES

LIST OF FIGURES

FIGURES

LIST OF SYMBOLS

c	Chord length
C_l	Sectional lift coefficient
C_d	Sectional drag coefficient
C_P	Power coefficient
C_Q	Torque coefficient
C_T	Thrust coefficient
D	Drag force
h	Sensible enthalpy
k	Thermal conductivity, turbulence kinetic energy
L	Lift force
p	Pressure
R	Rotor radius
r	Normalized radial distance from the rotational axis
y	Radial distance from the rotational axis
α_{TPP}	Tip path plane angle
β	Flapping angle
ε	Turbulence dissipation rate
μ	Dynamic viscosity, advance ratio
ρ	Density
Ω,ω	Rotational speed

Other parameters are clearly defined wherever applicable.

CHAPTER 1

INTRODUCTION

1.1 BACKGROUND

Flow fields of helicopters incorporate complex aerodynamic characteristics and are inherently unsteady, mainly due to the existence of rotors. The dynamic pressure is high at the blade tips; the aerodynamic forces concentrate there creating blade tip vortices. These vortices are transported downward and form helix shaped paths in hover [1]. In forward flight, these vortices can interact with the advancing blades and hence fluctuating airloads. This phenomenon is known as the blade vortex interaction [1].

Several other interactions exist including the ones between main rotor wake, fuselage, tail rotor wake, and engine plume. These interactions are schematically illustrated in Figure 1.

Furthermore, on the advancing side of the rotor, Mach numbers of typically 0.6-0.7 are reached introducing compressibility effects. The blades are flexible, and therefore, the aeroelastic effects are also quite common.

In addition to these phenomena, hot exhaust gases interact with the rotor wake and fuselage. Consequently, thermal effects must also be considered for the helicopter systems under path of the exhaust gases. In addition, the infrared (IR) signature of the helicopter becomes of great concern against military threats. The effect of the engine exhaust plume upon the fuselage can be observed from IR images, for example in Figure 2 to Figure 4 for the AH-1W helicopter in hover, and in flight at 60 knots and 120 knots [2], respectively.

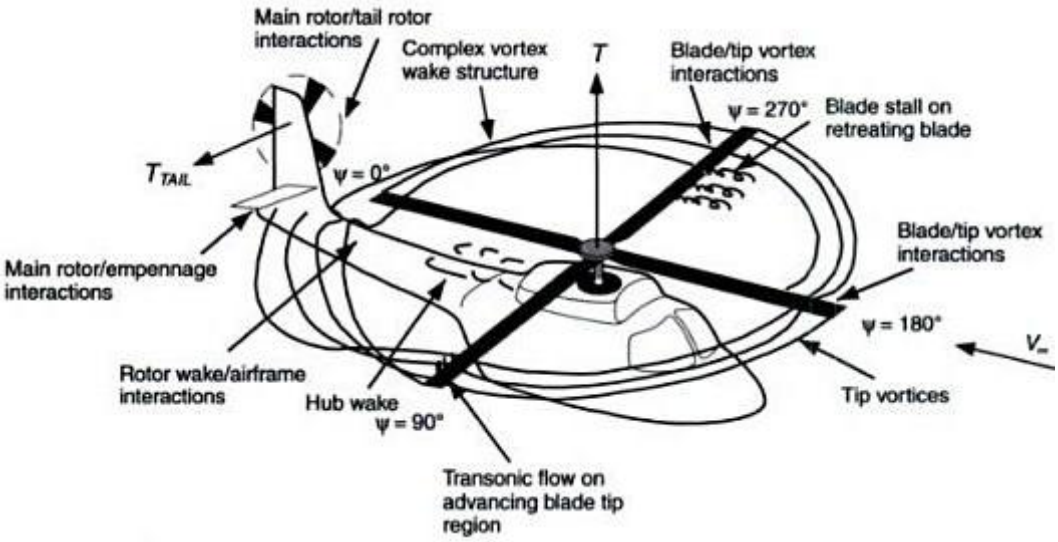

Figure 1 – Interactions in a helicopter [1]

Figure 2 – IR image of AH-1W in hover [2]

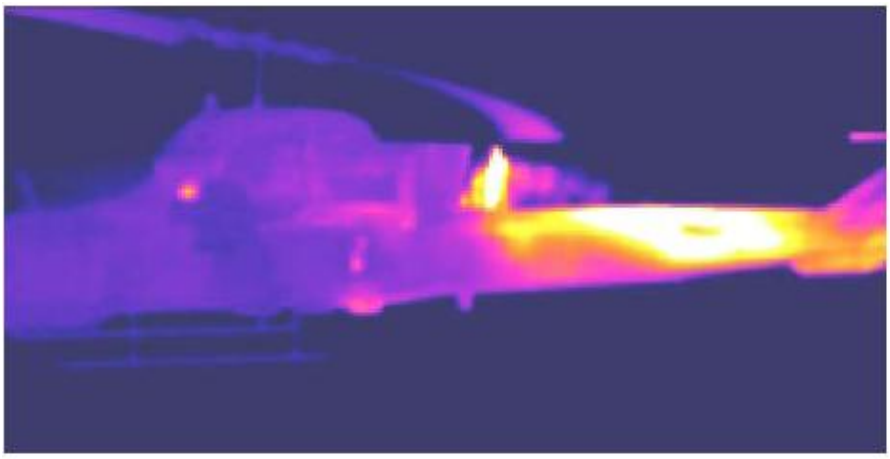

Figure 3 – IR image of AH-1W at 60 KIAS [2]

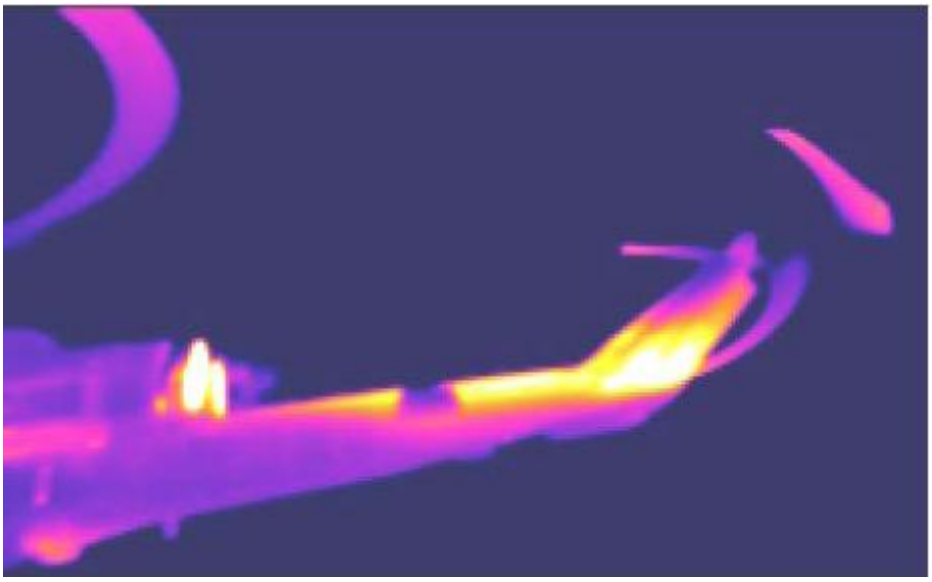

Figure 4 – IR image of AH-1W at 120 KIAS [2]

Prediction of helicopter aerodynamics accurately is of great importance due to its obvious influence on the helicopter's performance and handling qualities, structural and thermal loads, vibration and noise properties as well as the IR signature. However, obtaining the flow field of a helicopter is a challenging process due to its complexity. According to the type of the application, some interactions are

neglected in the analyses. Most of the wind tunnel tests and numerical applications ignore the effects of the engine and concentrate only on the influence of the rotors. Flight tests are costly and can be conducted at the very end of the design or modification phase. Nevertheless, computational fluid dynamics (CFD) is a means to predict the helicopter flow field fast and at a relatively low cost allowing the analysis of many possible configurations and flight conditions before the final design or modification.

1.2 LITERATURE REVIEW

From CFD point of view, a helicopter can be considered mainly as a combination of rotors, fuselage and engine. Approaches concentrate on one or more of these three elements.

Numerical analysis of fuselage alone is relatively straightforward since it is not different from modeling of the fixed wing aircraft, and there is a great deal of work done in this field of CFD. In a study by Mineck [3], the flow field about the generic helicopter body ROBIN was analyzed utilizing an unstructured grid Navier-Stokes solver and compared to two structured-grid Navier-Stokes solvers and experimental data.

Many valuable pieces of work on rotor/airframe interactions have been done. Berry et al. [4] assessed two different computational methods in low speed flight which account for the interaction of rotor and fuselage. In this study, the first method accounted for the rotor body interaction by a procedure that consisted of the selection of rotor performance parameters giving the desired thrust coefficient and calculation of the induced flow on the fuselage by the rotor. Then a correction of the collective and swashplate deviation by defining the fuselage effect on the rotor was included and finally a redefinition of the pressure distribution on the fuselage with the corrected rotor parameters was achieved. The second method utilized an incompressible Navier Stokes solver and simulated the rotor by a pressure jump at the rotor disk which was based on blade element theory. Park et al. [5] developed a three-dimensional parallel unstructured grid Euler solver to

predict the unsteady flow field of rotor-body combinations accounting for their interactions using a sliding mesh algorithm. O'Brien [6] implemented actuator disk, actuator blade, and overset models to a CFD solver for complete rotorcraft configuration simulations.

Literature on the engine effects on helicopter flow fields is relatively limited. O'Brien et al. [7] added engine modeling capability to a Reynolds Averaged Navier Stokes (RANS) solver to help investigate the engine effects on helicopter aeromechanics by coupling a one-dimensional engine program to the code by the use of inlet and exhaust boundary conditions. Cao, Su and Zhang [8] investigated the effect of rotor cross flow on the engine jet. The study of Dimanlig et al. [9] was intended to include the engine inlet and exhaust flow in the helicopter simulations, in particular for the Comanche helicopter, using overset type grids. However, the study was not completed.

1.3 THESIS SCOPE

In this study, the flow fields of a medium-lift utility helicopter in forward flight and hover are simulated through CFD accounting for the effects of exhaust hot gases. These effects are included through the engine exit boundary conditions. The work concentrates on the temperature distribution around the tail boom in particular. Analyses are performed for forward flight conditions at four different advance ratios; 0.07, 0.14, 0.19, 0.28 and hover in ground effect. The temperature field around the tail is compared with available flight test data.

The numerical solutions are carried out using the commercial computational fluid dynamics software ANSYS Fluent [10] incorporating a user defined function (UDF) [10] called Virtual Blade Model (VBM) [17] to account for the time-averaged rotor effects.

Chapter 1 of the thesis gives brief background information on the helicopter flow field analysis. Literature review on this subject is included in this chapter. Theoretical information related to the thesis work is given in Chapter 2. In this

chapter, fundamentals of rotor aerodynamics and performance are summarized. In Chapter 3, the numerical method and the flow solver employed for the analyses are described. This chapter also describes the grid generation procedure, governing equations, rotor modeling, solution set up, and boundary conditions. The results of all the cases investigated are presented and discussed in Chapter 4. The temperature distributions obtained are compared to the available flight test data. Finally, Chapter 5 includes some concluding remarks.

CHAPTER 2

THEORETICAL BACKGROUND

2.1 ROTOR FLOW ENVIRONMENT

The flow fields for the hover and forward flight cases are quite different from each other. While in hover the velocity distribution on the rotor is azimuthally axisymmetric as depicted in Figure 5, this is not the case for forward flight due to the combined effects of the rotor motion and free stream.

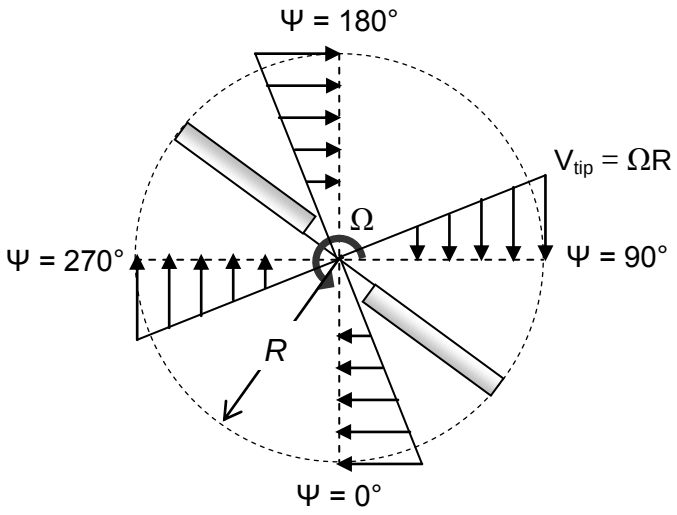

Figure 5 – Velocity distribution over the rotor in hover

Air is entrained into the rotor and a slipstream is formed. The flow velocity increases smoothly through the rotor and a pressure jump is resulted corresponding to the thrust produced over the rotor disk. At the blade tips, vortices are formed (Figure 6), and they move along the rotor wake. The slipstream velocity

increases downstream leading to a contraction in the wake. A typical rotor wake in hover is shown in Figure 7.

Figure 6 – Blade tip vortices [11]

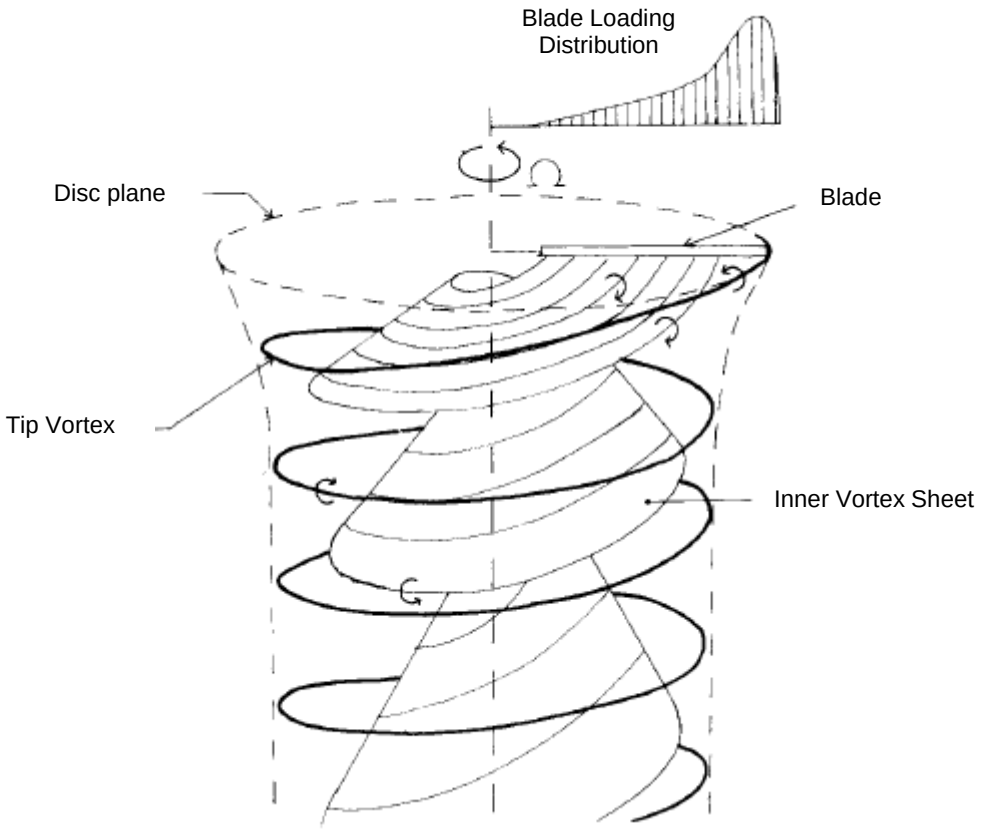

Figure 7 – Nature of total wake in hover [11]

In forward flight, the rotor disk is tilted forward to create a component of thrust in the flight direction in order to produce a propulsive force. In this case, with the existence of an onset velocity, the flow through the rotor is not azimuthally axisymmetric (Figure 8).

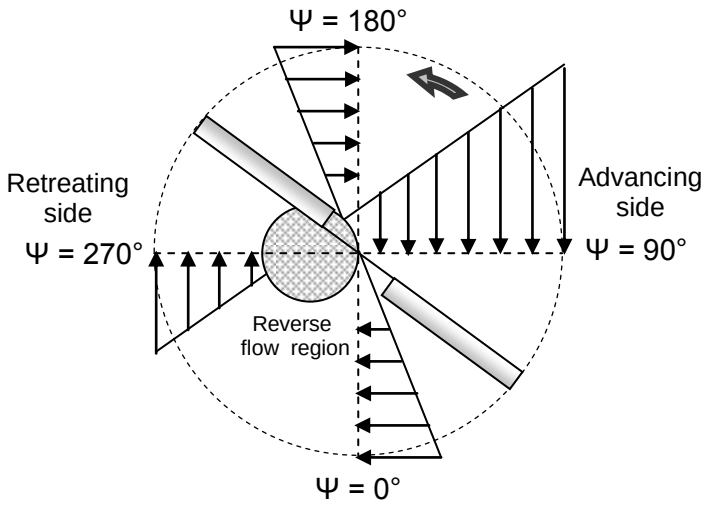

Figure 8 – Velocity distribution over the rotor in forward flight

On the advancing side where azimuth (denoted ψ) is between 0-180 degrees (measured from the tail direction counter clockwise), the free stream velocity adds to the rotational velocity, while on the retreating side where azimuth is between 180 and 360 degrees, the directions of free stream velocity and rotational velocity are opposite. There is also a reversed flow region within the retreating side, up to the point where the rotational speed equals the free stream velocity. This velocity distribution leads to a non-uniform dynamic pressure distribution that results in a lift imbalance between the two sides. This results in a large rolling moment. To overcome this imbalance the incidence of the blades are adjusted accordingly by the so called flapping motion.

2.2 ROTOR PERFORMANCE

Basic investigation of rotor performance in both hover and forward flight can be carried out using two approaches: momentum theory and blade element method. Momentum theory accounts for the rotor as a disk without dealing with the details of the flow field whereas in blade element method sectional aerodynamic loads are computed accounting for the chord, twist and airfoil shape. The Virtual Blade

Model (VBM) used in this thesis adopts momentum theory and blade element method.

2.2.1 MOMENTUM THEORY

Momentum theory is based on the actuator disk concept, which assumes that the rotor is an infinitesimally thin disc with a pressure jump across it. This approach assumes that the flow is inviscid, incompressible, one dimensional and quasi-steady through the rotor [1]. Then the theory relates thrust to the induced velocity through the use of conservation of mass, momentum and energy equations around a control volume including the rotor slipstream as shown in Figure 9 for hover case. Similarly, in forward flight, Glauert's approach is utilized, where the rotor is assumed in a slipstream as shown in Figure 10 and the analysis is performed with respect to the axes aligned with the rotor disk [1].

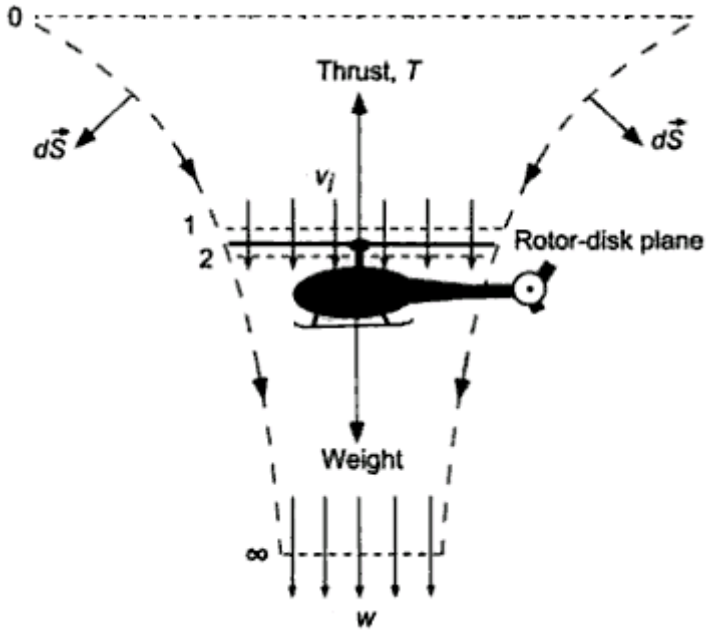

Figure 9 – Control volume used in momentum theory for hover [1]

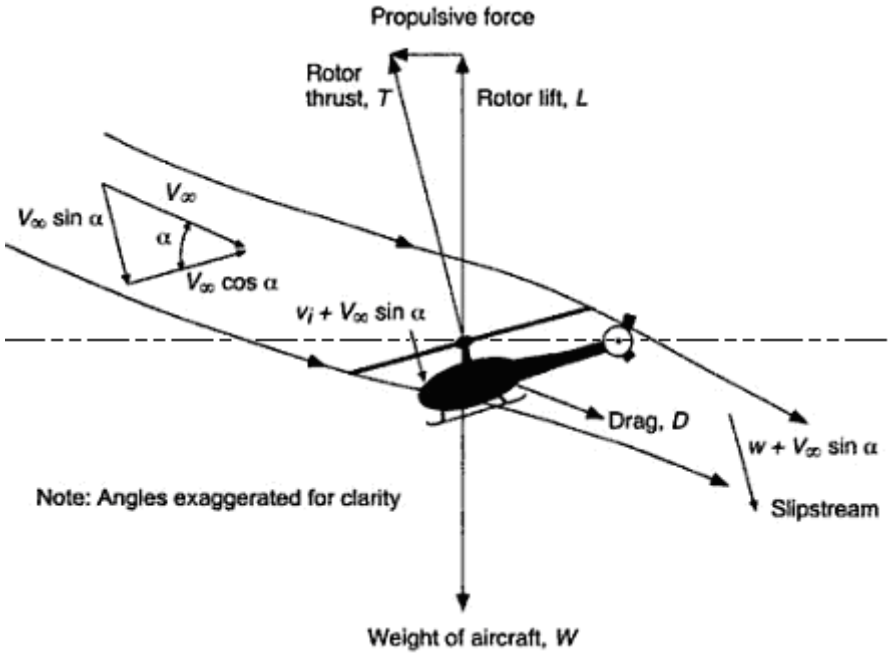

Figure 10 – Rotor slipstream used in momentum theory for forward flight [1]

2.2.2 BLADE ELEMENT THEORY

Blade element theory (BET) is based on the calculation of aerodynamic forces and moments on 2D sections of the blade (Figure 11) and then integration over the span and averaging the result over the rotor revolution. With this method radial and azimuthal aerodynamic loading on the blade can be predicted. This theory also accounts for the effects of airfoil shape, twist, and planform distribution [1].

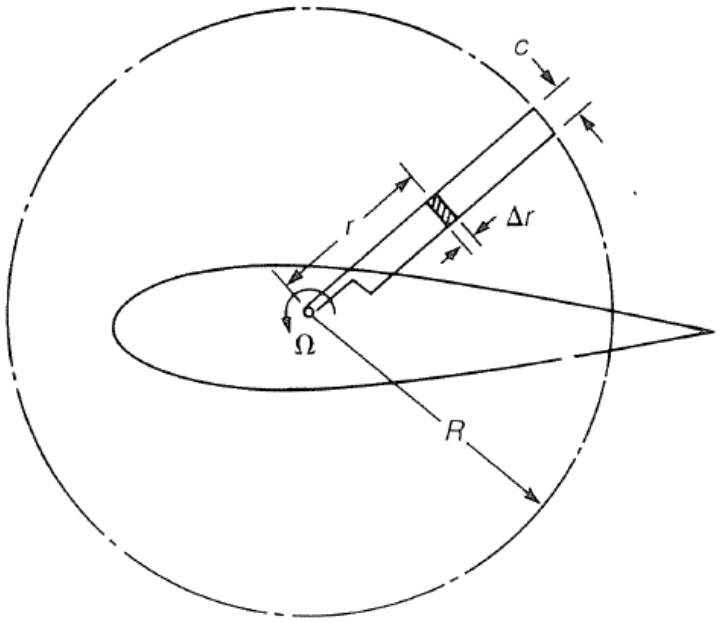

Figure 11 – Blade element geometry [12]

For hover the resultant velocity U at a blade element, located at a radial distance y from the center of rotation, can be resolved into two components; normal and parallel to the rotor, U_P and U_T, respectively, as depicted in Figure 12. Then the following relations can be established [1].

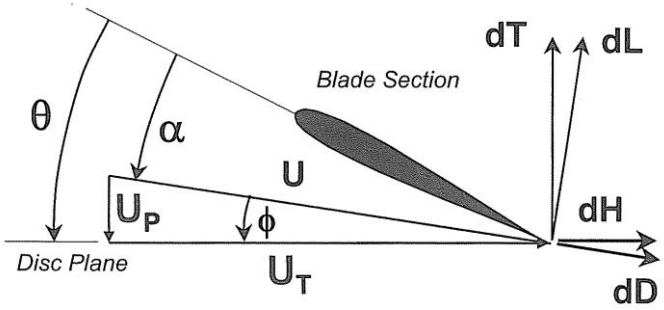

Figure 12 – Blade element in hover [11]

$$U_P = v_i \tag{1}$$

$$U_T = \Omega y \tag{2}$$

where v_i is the induced velocity.

The induced angle of attack is then [1]

$$\phi = \tan^{-1}\left(\frac{U_P}{U_T}\right) \tag{3}$$

For small angles [1]

$$\phi = \tan^{-1}\left(\frac{U_P}{U_T}\right) \approx \frac{U_P}{U_T} \tag{4}$$

The effective angle of attack α with θ being the pitch angle at the blade element is [1]

$$\alpha = \theta - \phi = \theta - \frac{U_p}{U_T} \tag{5}$$

Incremental thrust dT, torque dQ and power dP can be expressed in terms of lift and drag forces as [1]:

$$dT = dL\cos\phi - dD\sin\phi \tag{6}$$

$$dQ = (dL\sin\phi + dD\cos\phi)y \tag{7}$$

$$dP = (dL\sin\phi + dD\cos\phi)\Omega y \tag{8}$$

U_P is much smaller than U_T i.e. $U \approx U_T$. Small induced angle Φ leads to $\sin\phi \approx \phi$ and $\cos\phi \approx 1$ [1].

Since the drag is at least one order lower than lift the contribution and Φ is small, $dD\sin\phi \approx dD\phi$ can be neglected [1].

With these simplifications [1]

$$dT = dL \tag{9}$$

$$dQ = (\phi dL + dD)y \tag{10}$$

$$dP = (\phi dL + dD)\Omega y \tag{11}$$

Furthermore, non-dimensional quantities can be introduced [1]:

$$r = \frac{y}{R} \tag{12}$$

$$\frac{U}{\Omega R} = \frac{\Omega y}{\Omega R} = \frac{y}{R} = r \tag{13}$$

The incremental thrust, torque and power coefficients (dC_T, dC_Q, dC_P) are defined as follows [1]:

$$dC_T = \frac{dT}{\rho A(\Omega R)^2} \tag{14}$$

$$dC_Q = \frac{dQ}{\rho A(\Omega R)^2 R} \tag{15}$$

$$dC_P = \frac{dP}{\rho A(\Omega R)^3} \tag{16}$$

The inflow ratio can be defined as [1]:

$$\lambda_i = \frac{v_i}{\Omega R} = \frac{v_i}{\Omega y}\left(\frac{\Omega y}{\Omega R}\right) = \frac{U_P}{U_T}\left(\frac{y}{R}\right) = \phi r \tag{17}$$

Incremental lift and drag can be written as [1]

$$dL = \frac{1}{2}\rho U^2 c C_l dy \tag{18}$$

$$dD = \frac{1}{2}\rho U^2 c C_d dy \tag{19}$$

Accounting for the blade number, N_b, incremental thrust coefficient can be written as [1]

$$dC_T = \frac{N_b dL}{\rho A(\Omega R)^2} = \frac{N_b(\frac{1}{2}\rho U_T^2 c C_l dy)}{\rho(\pi R^2)(\Omega R)^2}$$
$$= \frac{1}{2}\left(\frac{N_b c}{\pi R}\right) C_l \left(\frac{y}{R}\right)^2 d\left(\frac{y}{R}\right) \quad (20)$$
$$= \frac{1}{2}\left(\frac{N_b c}{\pi R}\right) C_l r^2 dr$$

where $\sigma = \frac{N_b c}{\pi R}$ is the solidity.

Therefore the incremental thrust and torque (power) coefficients can be written as [1]

$$dC_T = \frac{1}{2}\sigma C_l r^2 dr \quad (21)$$

$$dC_P \equiv dC_Q = \frac{dQ}{\rho A(\Omega R)^2 R} = \frac{N_b(\phi dL + dD)y}{\rho(\pi R^2)(\Omega R)^2 R}$$
$$= \frac{1}{2}\left(\frac{N_b c}{\pi R}\right)(\phi C_l + C_d) r^3 dr \quad (22)$$
$$= \frac{1}{2}\sigma((\phi C_l + C_d) r^3 dr$$

Integrating the incremental coefficients from the blade root to the tip C_T, C_Q (C_P) are obtained.

In level forward flight, the tip path plane makes an angle α_{TPP} with the horizontal and considering the flow around a blade element on the rotor, the resultant velocity U on this blade element can be decomposed into three components as shown in Figure 13.

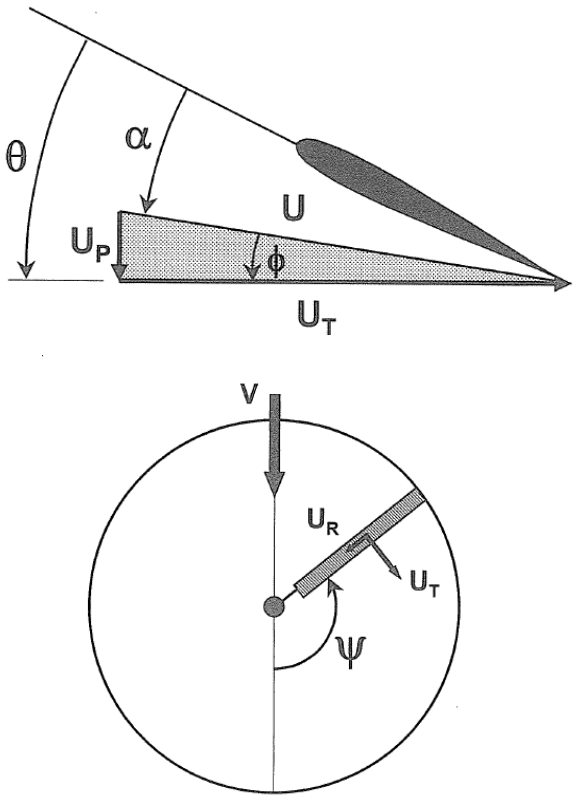

Figure 13 – Blade element in forward flight [11]

$$\vec{U} = \vec{U}_T + \vec{U}_p + \vec{U}_R \tag{23}$$

U_T, the tangential component to the rotor has a term due to the rotation of the blade and a translational part due to the forward flight [1].

$$U_T = U_T(y,\psi) = \Omega y + V_\infty \sin\psi \tag{24}$$

The perpendicular component to the blade U_P, has three terms. First one includes the inflow velocity whereas the other two result from the perturbations generated by flapping. The blade flapping velocity about the hinge produces $y(d\beta/dt)$ while coning creates $V_\infty \beta \cos\psi$ [1].

Since [11]

$$y\frac{d\beta}{dt} = y\frac{d\beta}{d\psi}\frac{d\psi}{dt} = y\Omega\frac{d\beta}{d\psi} \tag{25}$$

Then,

$$U_P = U_P(y,\psi) = V_\infty \sin\alpha_{TPP} + v_i + y\Omega\frac{d\beta}{d\psi} + V_\infty\beta\cos\psi \tag{26}$$

The radial component U_R is [11]

$$U_R = U_R(\psi) = V_\infty\cos\psi \tag{27}$$

A similar approach to that used for hover is followed, further assuming that U_R, as well as U_P, is much smaller than U_T i.e. $U \approx U_T$ and defining quantities specific to forward flight.

Advance ratio μ is

$$\mu = \frac{V_\infty\cos\alpha_{TPP}}{\Omega R} \approx \frac{V_\infty}{\Omega R} \tag{28}$$

Inflow factor for forward flight is [11]

$$\lambda = \frac{V_\infty\sin\alpha_{TPP} + v_i}{\Omega R} = \mu\alpha_{TPP} + \lambda_i \tag{29}$$

Normalized velocity components are [11]

$$u_T = r + \mu\sin\psi \tag{30}$$

$$u_P = \lambda + \beta\mu\cos\psi + r\frac{d\beta}{d\psi} \tag{31}$$

$$u_R = \mu\cos\psi \tag{32}$$

The incremental thrust coefficient is [11]

$$dC_T = \frac{1}{2}\sigma u_T^2 C_l dr \tag{33}$$

The incremental power (torque) coefficient is

$$dC_P \equiv dC_Q = \frac{1}{2}\sigma u_T^2 (\phi C_l + C_d) r dr = \frac{1}{2}\sigma (r + \mu \sin\psi)^2 (\phi C_l + C_d) r dr \tag{34}$$

CHAPTER 3

NUMERICAL METHOD AND FLOW SOLVER

3.1 ANSYS FLUENT

ANSYS Fluent is a commercial CFD software package with finite volume based solvers. Capabilities of Fluent include a wide range of incompressible and compressible, inviscid, laminar and turbulent fluid flow problems. Both steady and unsteady analyses can be performed and transport phenomena like heat transfer and chemical reactions can be modeled [10].

Fluent is an unstructured solver and uses internal data structures for ordering grid elements and communication between cells. In 2D, quadrilateral and triangular cells are allowed and in 3D hexahedral, tetrahedral, pyramid, wedge, and polyhedral cells, single and multi-block structured meshes, hybrid meshes are accepted. Fluent also allows grids with hanging nodes. These are nodes on edges and faces that are not vertices of all the cells sharing those edges or faces [10]. Non-conformal boundaries (different node locations at the boundaries of neighboring sub-domains) are, as well, allowed [10]. Fluent has pre-processors GAMBIT [13] and TGrid [14] for the computational grid generation. Fluent also has parallel processing capability.

Additional features can be embedded in Fluent to some extent through user-defined functions (UDF).

3.2 GENERATION of COMPUTATIONAL GRID

All unstructured computational grids used in this thesis are produced using preprocessors of Fluent. Surface mesh is formed in GAMBIT while surface mesh improvement and volume meshes are produced in TGrid.

A typical computational domain used in the investigations includes two sub-domains: main and tail rotor fluid zones. The process of generating this domain consists of three sub-processes: fuselage meshing, rotor meshing and generation of the surrounding flow domain grid.

Since the fuselage pitch angle and tip path plane of the main rotor varies with flight velocity, a different computational grid in terms of the orientations of the helicopter components is prepared for each analysis.

3.2.1 MODELING THE FUSELAGE

In the following subsections, the mesh generation procedures followed in this thesis are described in somewhat more detail.

3.2.1.1 SURFACE MESH GENERATION

First, the fuselage CAD model was imported into GAMBIT in the IGES format. The model was modified in order to eliminate details that were unnecessary for an aerodynamic analysis and to generate better quality mesh. Triangular elements were used in fuselage surface. Control of the growth size was handled by size function tool of GAMBIT [13].

In curved, intricate regions of the geometry, curvature size function [13] was used. This tool allows the specification of the maximum angle between normals of the adjacent grid elements [13]. On leading and trailing edges of horizontal tail, vertical tail, engine inlet and exhaust faces and around, up on tail boom where the temperature field was examined and around regions where high gradients of flow variables were expected, the mesh was kept finer than other regions. Two different mesh configurations were generated to check the mesh independence. Figure 14 and Figure 15 show the tail boom surface meshing for the two mesh configurations. The rounded mesh sizes are given in Table 2.

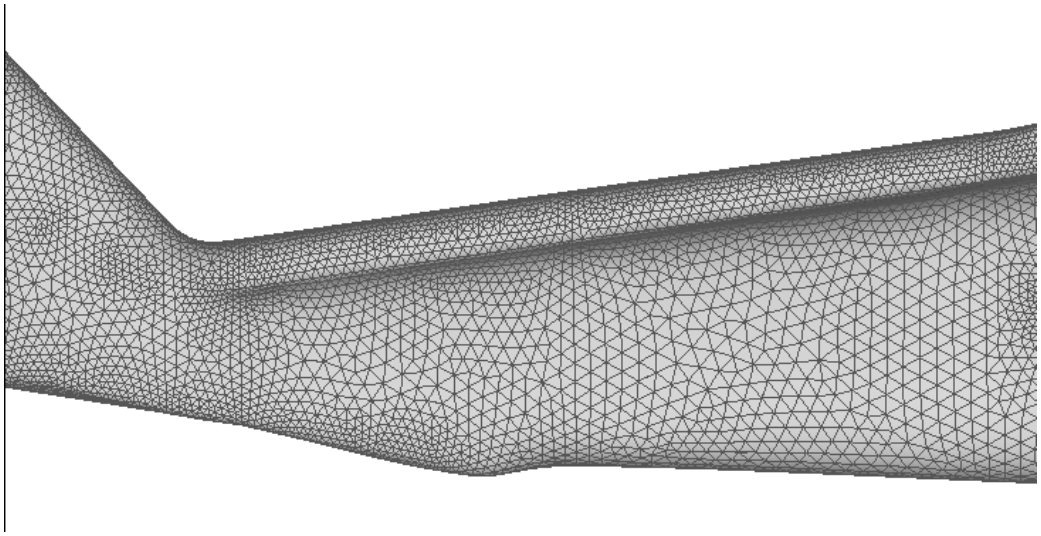

Figure 14 – Tail boom surface mesh of coarse mesh configuration

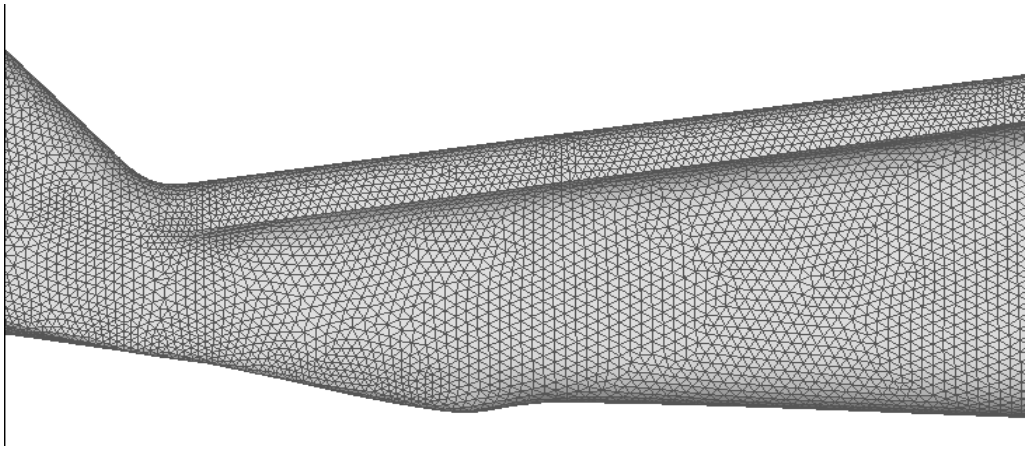

Figure 15 – Tail boom surface mesh of fine mesh configuration

Surface mesh quality was improved in TGrid by applying modifications like smoothing, merging cells, swapping edges. Mesh quality values are given in Table 3.

3.2.1.2 BOUNDARY LAYER GENERATION

The boundary layer mesh was generated in TGrid. The method called last ratio [14] was employed which adjusts the height of the last row of the boundary layer so that it will reach a prescribed percentage of the edge size of the surface mesh and the transition from the boundary layer to the tetrahedral volume cells will be smooth. Therefore, the boundary layer thickness varies throughout the surface grid. The maximum possible number of layers and thickness were achieved without diminishing the quality of the mesh. The first thickness was determined such that y-plus distribution up on the fuselage surface was between 30 and 300. Selection of this range of y-plus values brought about a requirement for near wall treatment. First layer thickness was not reduced to values on the order of 1, which would yield cell sizes requiring the use of double precision mode. The resultant boundary layer mesh properties are given in Table 1, while mesh size information is given in Table 2. Figure 16 shows the boundary layer mesh details for the coarse mesh configuration.

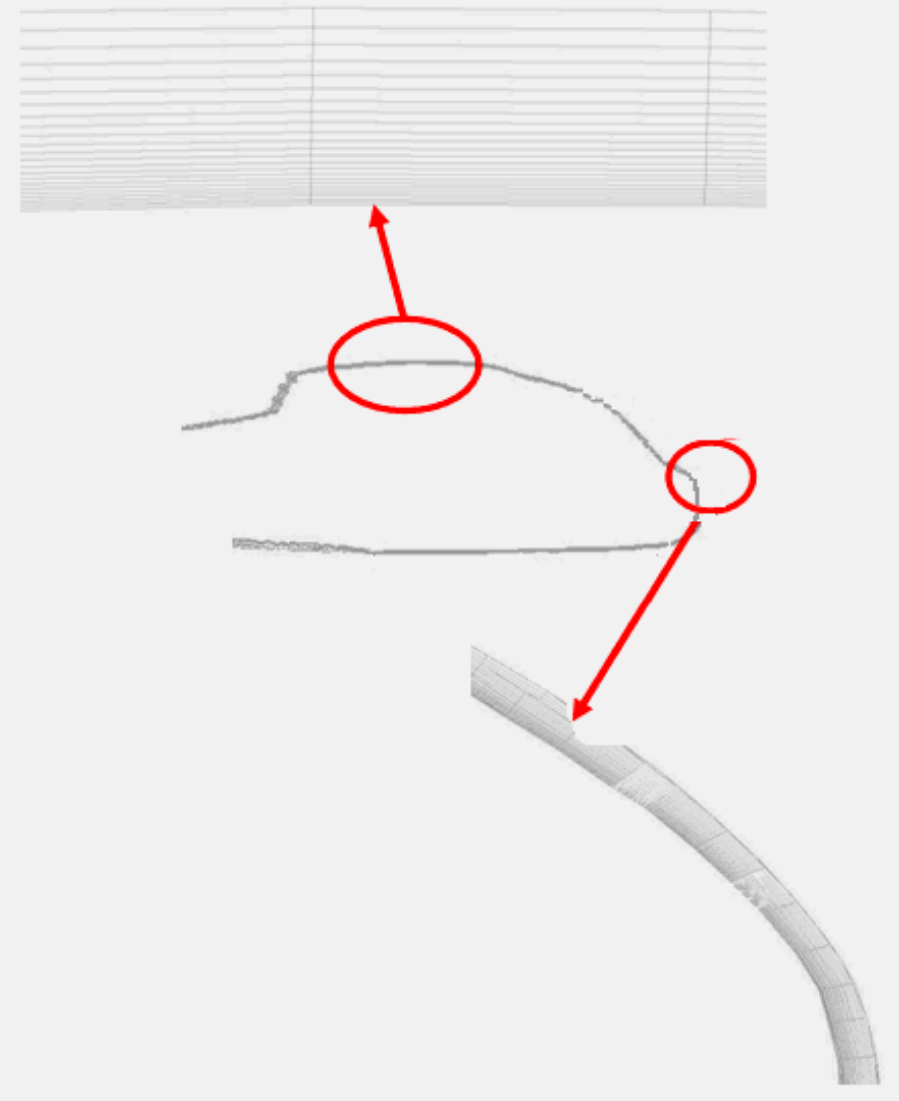

Figure 16 – Boundary layer grid of fuselage

Table 1 – Boundary layer properties

	MESH 1 (Coarse Mesh)	MESH 2 (Fine Mesh)
First layer thickness (m)	0.0025	0.0025
Number of layers	23	20
Last layer height/ edge size ratio	0.4	0.4

3.2.2 ROTOR MESH GENERATION

In VBM, the rotors are modeled as cylindrical fluid zones, and therefore, the blades are not included in the computational grid. In this study, the pave scheme [13] was used for the surface mesh generation of both rotors. The volume mesh was generated using the Cooper Scheme [13]. The main rotor mesh of the coarse mesh configuration is shown in Figure 17 and Figure 18. The resultant mesh size information is given in Table 2.

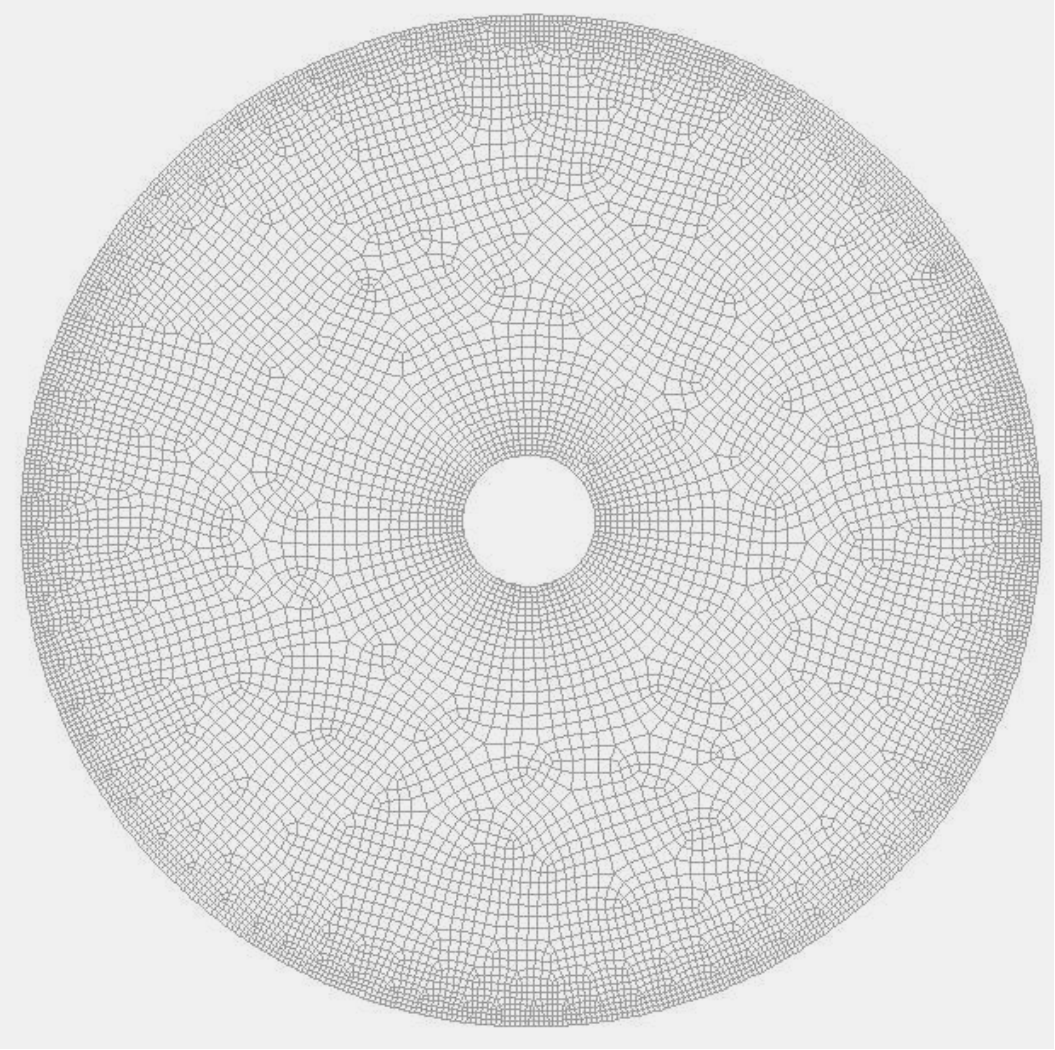

Figure 17 – Main rotor mesh – top view (coarse mesh)

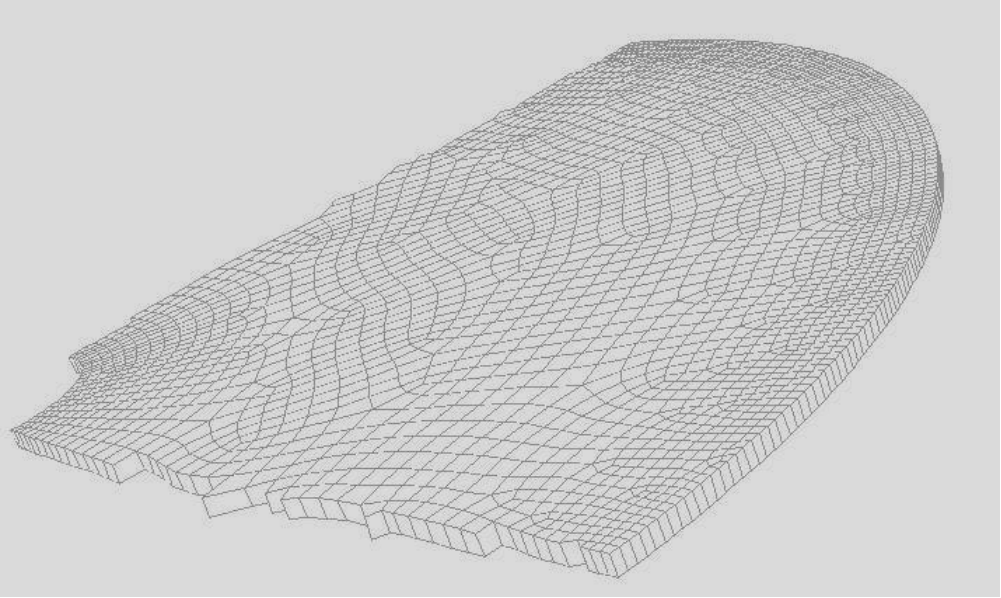

Figure 18 – Main rotor mesh – cut-out view (coarse mesh)

3.2.3 GENERATION of the FLOW DOMAIN MESH

The flow domain surrounding the helicopter was formed such that the flow will reach free stream conditions at the boundaries. The flow domain extends 5 rotor diameters upstream, left, right and above the helicopter, 10 rotor diameters downstream and below the helicopter. In addition, from upstream to downstream the flow domain was enlarged with a slope of 5.5 degrees on all outer side faces to make sure the flow enters the domain there so that these sides could be specified as inlet boundaries.

The flow domain was filled with tetrahedral elements. Since the rotor meshes consist of quadrilateral cells, the transition was through 120° pyramid cells. The total numbers of volume elements for both grids, including pyramid and boundary layer cells, are given in Table 2. The flow domains for forward flight and hover in ground effect cases are shown for the coarse mesh configuration in Figure 19 and Figure 20.

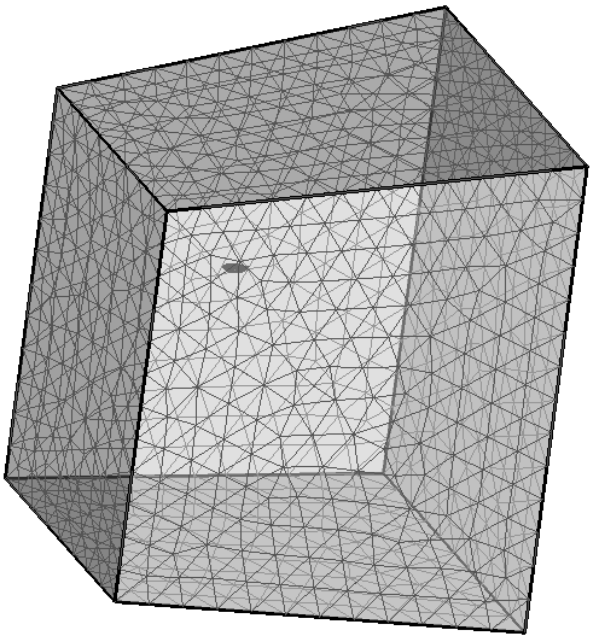

Figure 19 – Flow domain mesh – forward flight case (coarse mesh configuration)

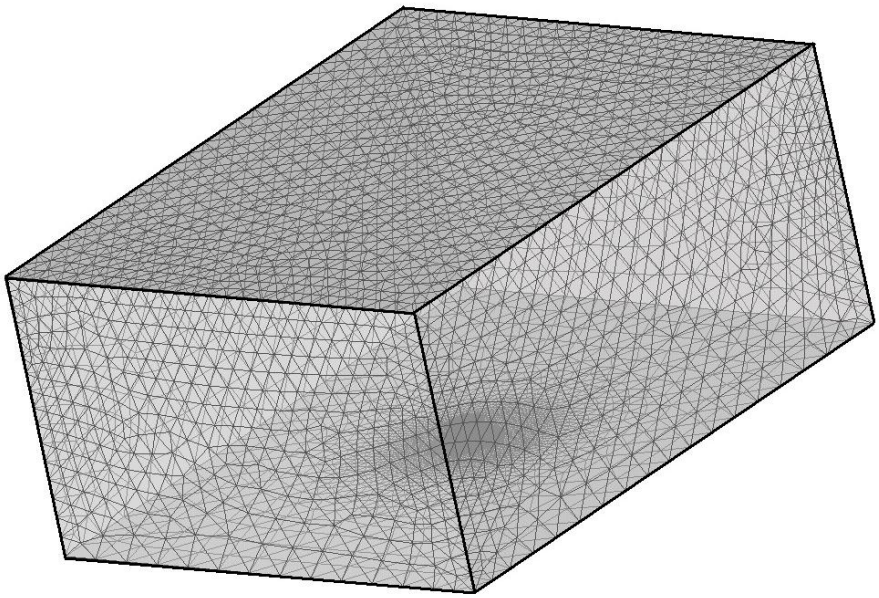

Figure 20 – Flow domain mesh – hover in ground effect case (coarse mesh configuration)

Table 2 – Mesh sizes for coarse and fine grids

	MESH 1 (Coarse Mesh)	MESH 2 (Fine Mesh)
Fuselage Surface Mesh	106 000	151 300
Main Rotor Surface Mesh	14 500	20 000
Tail Rotor Surface Mesh	5 000	7 000
Main Rotor Volume Mesh	7 000	9 600
Tail Rotor Volume Mesh	2 400	3 300
Boundary Layer	2 460 000	3 026 000
Volume Mesh (total, including boundary layer mesh and rotor meshes)	5 780 000	10 105 000

Table 3 – Mesh skewness values for coarse and fine meshes

		MESH 1 (Coarse Mesh)	MESH 2 (Fine Mesh)
Fuselage Surface Mesh	Maximum Skewness	0.78	0.65
	Average Skewness	0.035	0.022
Volume Mesh	Maximum Skewness	0.93	0.94
	Average Skewness	0.27	0.23

3.3 GOVERNING EQUATIONS

In Fluent, conservation of mass and momentum are solved for all flows. Should the flow involve heat transfer or compressibility, energy equation is solved as well. Fluent solves additional transport equations for turbulent flows [10].

The helicopter flow field is turbulent; therefore, in all the numerical investigations turbulence was accounted for. Reynolds-averaging was adopted. Hence the continuity equation solved is [10]

$$\frac{\partial \rho}{\partial t} + \frac{\partial}{\partial x_i}(\rho u_i) = 0 \tag{35}$$

Momentum equation (Reynolds averaged Navier-Stokes – RANS) is [10]

$$\frac{\partial}{\partial t}(\rho u_i) + \frac{\partial}{\partial x_j}(\rho u_i u_j) = -\frac{\partial p}{\partial x_i} + \frac{\partial}{\partial x_j}\left[\mu\left(\frac{\partial u_i}{\partial x_j} + \frac{\partial u_j}{\partial x_i} - \frac{2}{3}\delta_{ij}\frac{\partial u_k}{\partial x_k}\right)\right] + \frac{\partial}{\partial x_j}(-\rho\overline{u_i' u_j'}) \tag{36}$$

Energy equation accounting for the turbulence is [10]

$$\frac{\partial}{\partial t}(\rho E) + \frac{\partial}{\partial x_i}\left[u_i(\rho E + p)\right] = \frac{\partial}{\partial x_j}\left[\left((k + \frac{C_p \mu_t}{\mathrm{Pr}_t}\right)\frac{\partial T}{\partial x_j}\right] \tag{37}$$

where the total energy E is

$$E = h - \frac{p}{\rho} + \frac{u^2}{2} \tag{38}$$

Based on a series of solutions carried out with the ROBIN geometry using the Virtual Blade Model and different turbulence models, the realizable k-ε model was assessed to be a proper model to capture the flowfield of the helicopter. Therefore, in this study the realizable k- ε model was used.

k-ε model is a two equation turbulence model in which two separate transport equations are solved to determine the turbulent velocity and length scales. It is a

semi-empirical model proposed by Launder and Spalding. The realizable k-ε model is an improved variant of the standard k-ε model which has a new formulation for turbulent viscosity and a new transport equation for the dissipation rate. The realizable k- ε model predicts the spreading rates of planar and round jets more accurately and is superior in problems involving flows with rotation, boundary layers in adverse pressure gradients, separation and recirculation [10]. The transport equations for the realizable k-ε model are [10]

$$\frac{\partial}{\partial t}(\rho k)+\frac{\partial}{\partial x_j}(\rho k u_j)=\frac{\partial}{\partial x_j}\left[\left(\mu+\frac{\mu_t}{\sigma_k}\right)\frac{\partial k}{\partial x_j}\right]+G_k+G_b-\rho\varepsilon-Y_M+S_K \tag{39}$$

$$\frac{\partial}{\partial t}(\rho \varepsilon)+\frac{\partial}{\partial x_j}(\rho \varepsilon u_j)=\frac{\partial}{\partial x_j}\left[\left(\mu+\frac{\mu_t}{\sigma_\varepsilon}\right)\frac{\partial \varepsilon}{\partial x_j}\right]+\rho C_1 S_\varepsilon-\rho C_2\frac{\varepsilon^2}{k+\sqrt{\upsilon\varepsilon}}+C_{1\varepsilon}\frac{\varepsilon}{k}C_{3\varepsilon}G_b+S_\varepsilon \tag{40}$$

$$C_1=\max\left[0.43,\frac{\eta}{\eta+5}\right] \tag{41}$$

$$\eta=S\frac{k}{\varepsilon} \tag{42}$$

$$S=\sqrt{2S_{ij}S_{ij}} \tag{43}$$

where G_K represents the generation of turbulence kinetic energy due to the mean velocity gradients. G_b is the generation of turbulence kinetic energy due to buoyancy. Y_M represents the contribution of the fluctuating dilatation in compressible turbulence to the overall dissipation rate C_2 and $C_{1\varepsilon}$ are constants. σ_K and σ_ε are the turbulent Prandtl numbers for k and ε, respectively. S_k and S_ε and are user-defined source terms.

Non-equilibrium wall function was used with k- ε turbulence model. Non-equilibrium wall functions can partly include the pressure gradient effects and are recommended for complex flows involving separation, reattachment where severe pressure gradients and rapid changes exist in the mean flow and turbulence [10].

3.4 SOLVER

Fluent's pressure based solver is employed to solve the integral form of the governing equations for conservation of mass, conservation of momentum, energy and turbulence.

In the pressure based solver, continuity and momentum equations are manipulated to obtain a pressure equation yielding the pressure field [10]. The domain is divided into individual control volumes using the computational grid. The governing equations are integrated in each control volume to form algebraic equations for the discrete dependent variables (velocities, pressure, temperature etc.) The discretized equations are linearized and the resultant linear equation system is solved to obtain updated values of the dependent variables [10]. Finite-volume method is used for the discretization process. The solution procedure is outlined in Figure 21.

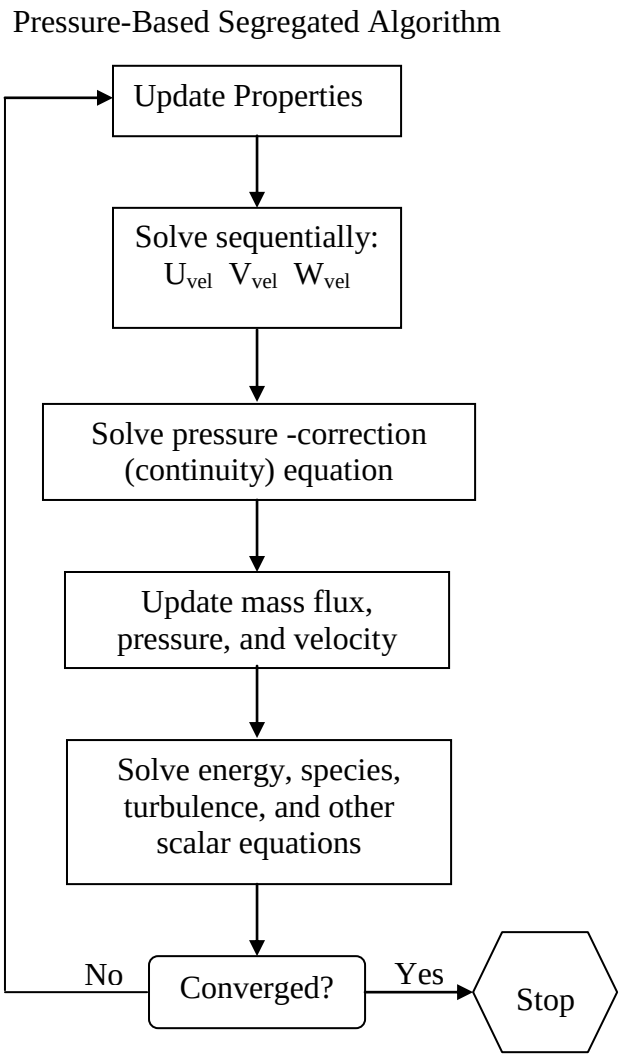

Figure 21 – Pressure Based Segregated Algorithm of Fluent [10]

3.4.1 SPATIAL DISCRETIZATION

In Fluent, the discrete values of scalars are stored at cell centers. These values are interpolated through upwind schemes to obtain the values at the face centers that are required for the convection terms. There are different upwind schemes in Fluent, including first order, second order, power law, and QUICK [10].

In this thesis, following the solution initialization, first iterations are performed employing first order upwind for all quantities to allow the flow to settle so as to avoid divergence. Then the solution is continued using second order upwind scheme and PRESTO! for pressure.

In the first order upwind scheme, the values at the cell centers are assumed to represent cell-average values so that the face quantities are taken equal to the cell-center quantities in the upstream cell [10].

In the second order upstream scheme, Taylor series expansion of the cell-center solution about the cell centroid is used to compute the face value [10].

$$\phi_{f,s} = \phi + \nabla\phi \bullet \vec{r} \qquad (44)$$

where Φ is the value to be computed.

PRESTO! (PREssure STaggerring Option), is a pressure interpolation scheme that uses the discrete continuity balance for a staggered control volume about the face to compute the face pressure so as to handle high pressure gradients encountered generally in rotating flows, high Rayleigh number natural convection, flows involving porous media [10].

3.4.2 EVALUATION OF GRADIENTS AND DERIVATIVES

For the calculation of scalars at the face values, secondary diffusion terms and velocity derivatives, gradients are required [10]. For this, the Green-Gauss node based evaluation method is employed.

3.4.3 UNDER-RELAXATION OF VARIABLES

In an effort to avoid divergence, under-relaxation factors are used to control the change of the variables computed in each iteration. Fluent allows the use of under-

relaxation factors. With under-relaxation factor α, the updated value of a variable is [10]

$$\phi = \phi_{old} + \alpha\Delta\phi \quad (45)$$

3.5 BOUNDARY CONDITIONS

The values of the boundary conditions of the flow domain surrounding the helicopter are obtained from the conditions of the flight tests which are used to validate the numerical analysis. The atmospheric pressure of the test location is taken as the operating pressure and the outside air temperature measured during the relevant test leg is used as the temperature. Flight velocity is utilized to compute the stagnation values.

3.5.1 PRESSURE INLET BOUNDARY CONDITION

Pressure inlet boundary condition is used to define the total pressure at flow inlets. In this thesis, pressure inlet boundary condition is used on all surrounding boundaries of the flow domain around the helicopter except for the one downstream. The total pressure is set to that of the free-stream. The inputs to this condition relevant to this study are

- Total pressure,
- Total (stagnation) temperature (for energy calculations),
- Flow direction,
- Turbulence parameters (for turbulent calculations),

3.5.2 PRESSURE OUTLET BOUNDARY CONDITION

When the pressure outlet boundary condition of Fluent is used, the static pressure at the outlet boundary is specified in conjunction with a set of back-flow conditions in case the flow reverses direction. Fluent extrapolates all other conditions from the interior of the domain [10]. In this study pressure outlet boundary condition is used on the downstream boundary of the flow domain around the helicopter. The static pressure and the total temperature are set to those of the free-stream.

The following inputs are used for the pressure outlet boundary conditions in this study.

- Static pressure
- Total temperature
- Backflow direction specification method
- Turbulence parameters (for turbulent calculations)

The user can specify the backflow direction or let Fluent determine the direction of the backflow using the direction of the flow in the cell layer adjacent to the pressure outlet. When backflow occurs, the static pressure specified is used as total pressure. The flow direction in this case is normal to the boundary [10].

3.5.3 MASS-FLOW INLET BOUNDARY CONDITION

Mass flow boundary condition is used to define a mass flow rate or mass flux distribution at an inlet. The total pressure is therefore permitted to vary in response to the interior solution to match the mass flow rate prescribed [10].

The inputs to this boundary condition relevant to this study are

- Mass flow rate,
- Total temperature,
- Flow direction,
- Turbulence parameters.

The helicopter analyzed in this study is a twin-engine configuration. The engines are included in the simulation as inlet and exhaust through mass flow inlet boundary conditions.

3.5.3.1 BOUNDARY CONDITIONS AT THE ENGINE INLETS

Mass flow inlet boundary condition is utilized for the inlet boundary. The direction of the flow is taken normal to the boundary face. The mass flow rate is evaluated utilizing available engine test data in light of the study of Ballin [15]. Reference [15]

gives the corrected mass flow rate at the compressor inlet versus the compressor static pressure ratio for different corrected compressor/ gas generator speed (Figure 22). In an effort to obtain these parameters, first the engine torque values corresponding to the flight speeds are obtained by utilizing the TRIM-CF code developed by Çalışkan [16]. Then, the compressor pressure ratio and corrected gas generator speeds are obtained versus engine torque from the available engine test data. The inlet total temperature is taken to be that of free-stream.

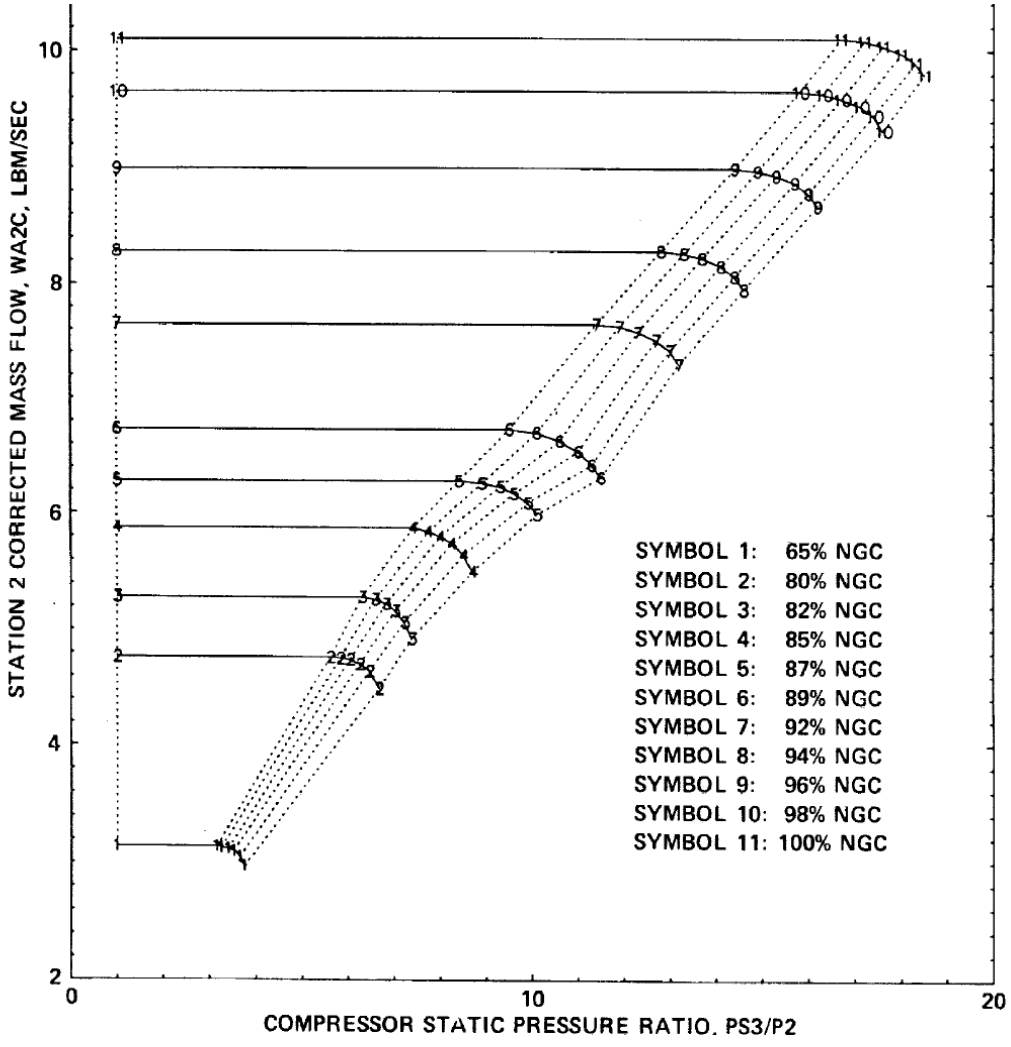

Figure 22 – Corrected compressor inlet mass flow rate versus compressor static pressure ratio for the T700 Engine [15]

3.5.3.2 BOUNDARY CONDITIONS AT THE EXHAUSTS

Mass flow inlet boundary condition is used for the exhaust boundary. The flow direction is taken normal to the boundary face. While determining the boundary condition values, the following assumptions are made:

- Exhaust gases are approximated as hot air.
- Mass flow rate of fuel is negligible next to that of air. Therefore the mass flow rate at the exhaust is taken equal to that at the inlet.
- Uniform temperature distribution is assumed throughout the exhaust face.

The exhaust gas temperature is approximated utilizing the available flight test data. During flight, the temperature at the turbine exit (TGT) was recorded. Furthermore, a separate ground test was conducted for the measurement of the exhaust temperature. The temperature at the center of exhaust was measured by a thermocouple and the TGT was recorded meanwhile. As a simple approximation, the difference between the two values was applied to the TGT values for the flight cases to obtain the corresponding temperatures at the exhaust.

Mass flow rate of fuel is neglected next to mass flow rate of air; therefore, exhaust mass flows rate is taken equal to inlet mass flow rate.

3.5.4 WALL BOUNDARY CONDITION

The fuselage is defined as an adiabatic wall with no slip condition. As a result of the adiabatic wall assumption it is expected that the wall temperatures would be higher than those of a conductive wall.

3.6 VIRTUAL BLADE MODEL

A helicopter rotor can be modeled employing different methods in Fluent. The boundary condition fan [10], which creates a pressure jump across the face it is assigned to, is one way of modeling the rotor. However, such a model would yield a very crude estimate of the flow field created by the rotor. A high accuracy

approach could be the utilization of the multiple rotating reference frame [10] or sliding mesh models [10]. In both of these methods, blades are included in the computational grid and they are located in a sub-domain (a cylindrical fluid volume) communicating with the global domain through the interface boundaries. Multiple reference frame (MRF) is a steady-state approximation and the relative motion of the rotating zone is not accounted for; the grid remains fixed. This is similar to freezing the motion of the moving part in a particular position and examining the instantaneous flow field [10].

In sliding mesh model, the rotating fluid sub-domain grid moves with time and this unsteady approach yields even more accurate results but is computationally more expensive. With the utilization of MRF or sliding mesh model, the rotation of the rotor could be modeled without accounting for the blade motions in the expense of high computational time and resources. Owing to the high aspect ratios of helicopter blades, it is easy to reach a surface mesh size from 70000 to 100000 on each blade, when the airfoil geometry was to be captured using sixty to eighty nodes. With a boundary layer of twenty rows, only the rotor boundary layer element size can reach eight million. The cell sizes near the surfaces decrease to orders of 10^{-11} to 10^{-13} which require the use of double precision computation thereby increasing the required computational time and resources even more.

With the addition of the dynamic meshing [10] and user-defined function [10] features of Fluent, such a dense mesh could yield highly accurate results, however. In dynamic meshing, the mesh deforms to perform a prescribed motion. The cells deform, and the mesh is updated in the deforming regions. Dynamic meshing in conjunction with the user defined functions enables the user to define the motion of the center of gravity of a zone (translation and rotation). Utilizing this feature, the blade flapping, feathering and lead-lag motions can be modeled as well as the rotation of the rotor. Dynamic meshing can be combined with the sliding mesh model thereby eliminating the need for modeling the rotation of the blade through the use of dynamic meshing. Such an analysis is inherently unsteady. Since the amplitudes of these motions are relatively small, the time step is at least

on the orders of 10^{-4} or 10^{-5} to capture the blade motion. A trial is performed in 16 parallel processors with an eight million size mesh yielding output files of exceeding 1.5GB in total. A transient analysis requires storage of files regularly. This approach is not followed due to time and computational resource limitations; and instead, Virtual Blade Model is adopted for the modeling of the rotors. Therefore, in this thesis the flow-field is investigated in a time-averaged fashion.

VBM implicitly models the time-averaged effect of the rotor on the flow field using source terms in the momentum equations located in a disk volume. It accounts for the effects of the blades without including them in the computational mesh. The mutual aerodynamic interaction between rotors and airframe is solved by coupling the VBM with the flow field equations of Fluent's Navier Stokes solvers. VBM has an embedded trimming algorithm [17].

3.6.1 NUMERICAL IMPLEMENTATION

The rotor blade source terms are unknown at the start. They develop as a part of the solution by the use of Blade Element Theory which requires the separation of the blade in spanwise sections. VBM allows the spanwise variation of chord length, airfoil, and twist [17].

Local angle of attack, Mach number, Reynolds number at each blade element are calculated using the computed velocity field. Then for each of these sections the local C_l, C_d values are obtained from the look up table. The instantaneous rotor forces are calculated in the form [17]:

$$f_{l,d} = C_{l,d}(\alpha, M, \mathrm{Re})\, c(r/R)\, \frac{\rho u_{tot}^2}{2} \tag{46}$$

where u_{tot} is the total lift/drag producing velocity component experienced by the blade cross section including the rotational speed Ω. Time averaging is equivalent to geometric averaging over 2π, assuming constant rotational speed. Therefore the time-averaged resultant forces in a cell is [17]:

$$F_{L,D,cell} = N_b \frac{\Delta r \, r \Delta \psi}{2\pi r} f_{l,d} \tag{47}$$

The time-averaged source term is then [17]

$$S_{cell} = -\frac{\vec{F}_{cell}}{V_{cell}} \tag{48}$$

This source term is added to the momentum equations, the flow field is updated and iterations proceed [17].

In VBM a rotor disk is identified by its origin pitch and bank angle (Figure 23) [17].

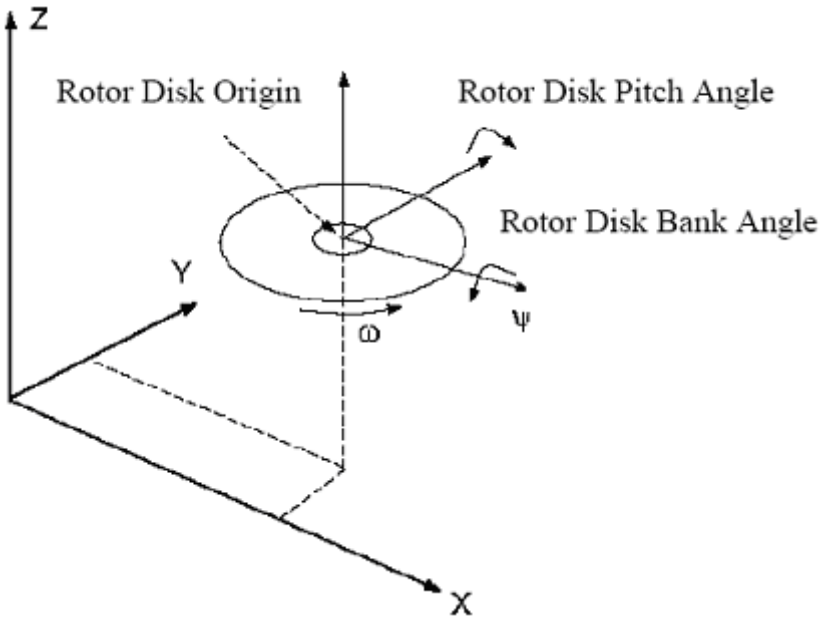

Figure 23 – Definition of rotor disk in VBM [17]

VBM defines the blade pitch as below [17]:

$$\theta = \theta_0 - \theta_{1c} \cos\psi - \theta_{1s} \sin\psi \tag{49}$$

The collective pitch θ_0, lateral cyclic θ_{1c}, and longitudinal cyclic θ_{1s} can be user-defined or computed by the trim routine [17].

3.6.2 TRIM ROUTINE

The implementation of non-linear relation between collective pitch and the thrust coefficient, and between the cyclic pitch and hub moments allows for the simulation of more than one rotor, therefore tail rotor can be simulated using VBM. VBM can compute the required pitch angles (collective and cyclic) for a desired thrust and zero moments around the hub [17].

3.6.3 BLADE FLAPPING

VBM takes flapping into account only if the user can provide coning β_0, longitudinal and lateral flapping coefficients β_{1c}, β_{1s}. The velocity components are transformed from the rotor shaft plane to the actual tip path plane to account for the coning and first harmonics (Figure 24) [17].

The resultant flapping angle is [17]

$$\beta = \beta_0 - \beta_{1c}\cos\psi - \beta_{1s}\sin\psi \tag{50}$$

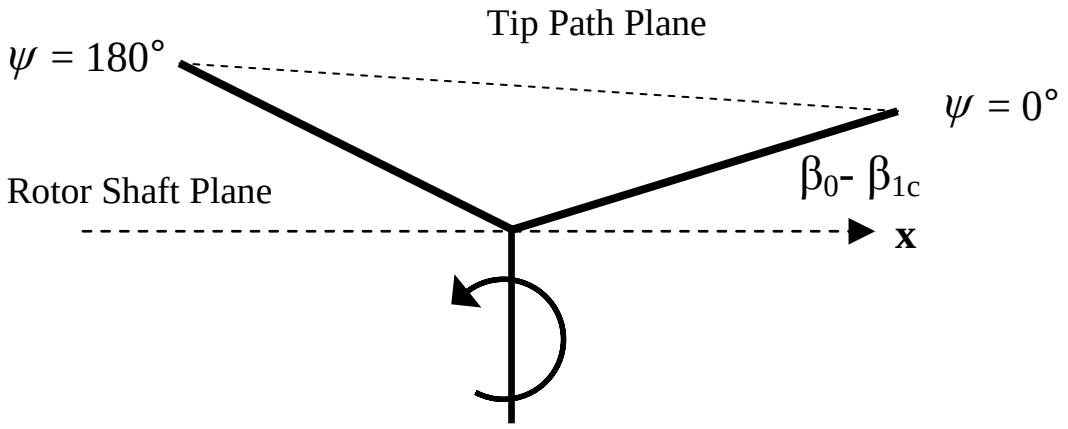

Figure 24 – Blade flapping angles as used in VBM [17]

3.6.4 BLADE GEOMETRY

VBM allows for spanwise variation of chord, twist and airfoil. The user defines these values as a function of normalized sections and the model assumes linear distribution of chord and twist in between two sections. As for the varying airfoil types, a linear interpolation is done for C_l and C_d between two defined sections. The model also interpolates C_l and C_d from the local conditions, using the C_l C_d values as a function of Mach number and Reynolds number in the look up tables [17].

3.6.5 TIP EFFECT

VBM takes the tip effect into account using a user-defined percentage. The lift is taken zero outward of the given percentage of the normalized span whereas the drag force is still calculated [17].

Ruith [17], validated VBM against experimental data performed with the model of Georgia Institute of Technology test. Good agreement was obtained.

CHAPTER 4

RESULTS and DISCUSSION

Analyses were run for a total of five cases: Four forward flight cases with advance ratios of μ=0.28, μ=0.19, μ=0.14, μ=0.07 and a hover case in ground effect (HIGE). In all these cases the flow fields were examined and the temperatures were extracted and compared to the available flight test data at 36 points. Post-processing of the results was performed in Tecplot 360 [18].

4.1 UTILIZATION OF THE FLIGHT TEST DATA

The temperature data used for comparison with numerical results were obtained from certain legs of a flight test in which temperature data were collected totally at 70 spatial points during a 80-minute flight profile. In this thesis, data from 36 of these points were used. Flight temperature data were acquired through thermocouples that were attached to the tips of 0.15 m rods placed perpendicularly to the tail boom surface. These rods were erected to the boom wall as four different sets on the right upper, right lower, left upper, and left lower sides of the boom (Figure 25). The temperature values were extracted from the computed flow fields at 0.15 m distance off the tail boom wall along the lines where the thermocouples were placed. These lines are shown in Figure 25. The data collected at one thermocouple are shown in Figure 26. The duration of the test legs used in this thesis changed from 27 seconds to 110 seconds which are given in Table 4. The data collected by thermocouples were transferred to two data acquisition systems. The data acquisition systems have 45 channels. The sampling rate for this study was 4Hz.

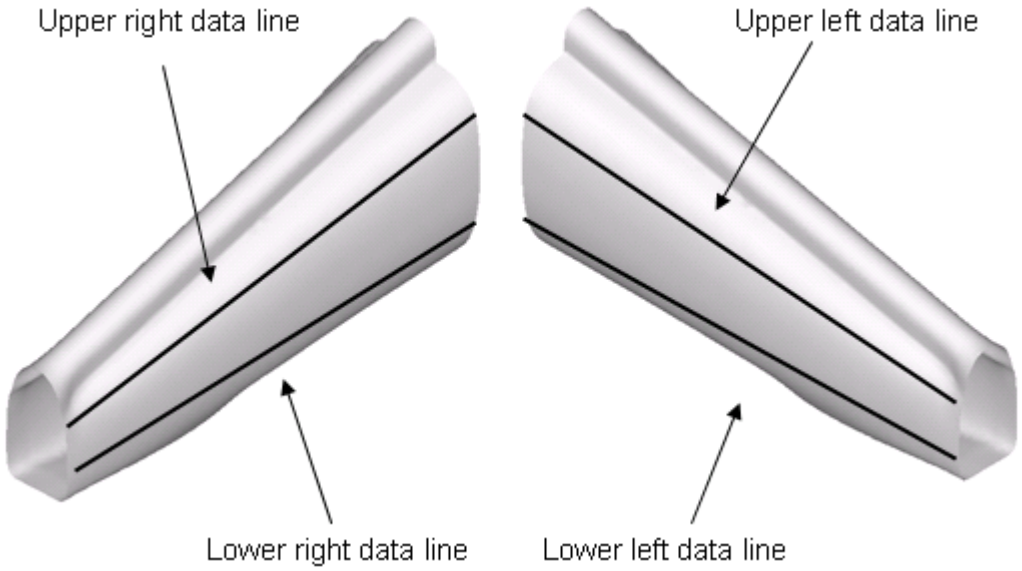

Figure 25 – Data lines on the tail boom. The data points lie along the lines shown.

Table 4 – Durations of the flight test legs used in this thesis

Flight Leg	Duration (min: sec)
HIGE	01:28
μ= 0.07	00:27
μ= 0.14	01:16
μ= 0.19	00:51
μ= 0.28	01:00

Since the flowfield is inherently unsteady, fluctuations were observed in the measured data. While in some legs large fluctuations in the measured data were observed, the fluctuations were quite limited in some others. Since the computed

results were based on RANS equations, an averaging procedure was used for comparison. Before averaging the flight data, the ones that showed sudden increases and decreases were eliminated. The raw data and the averaged data at one thermocouple position are plotted in Figure 27.

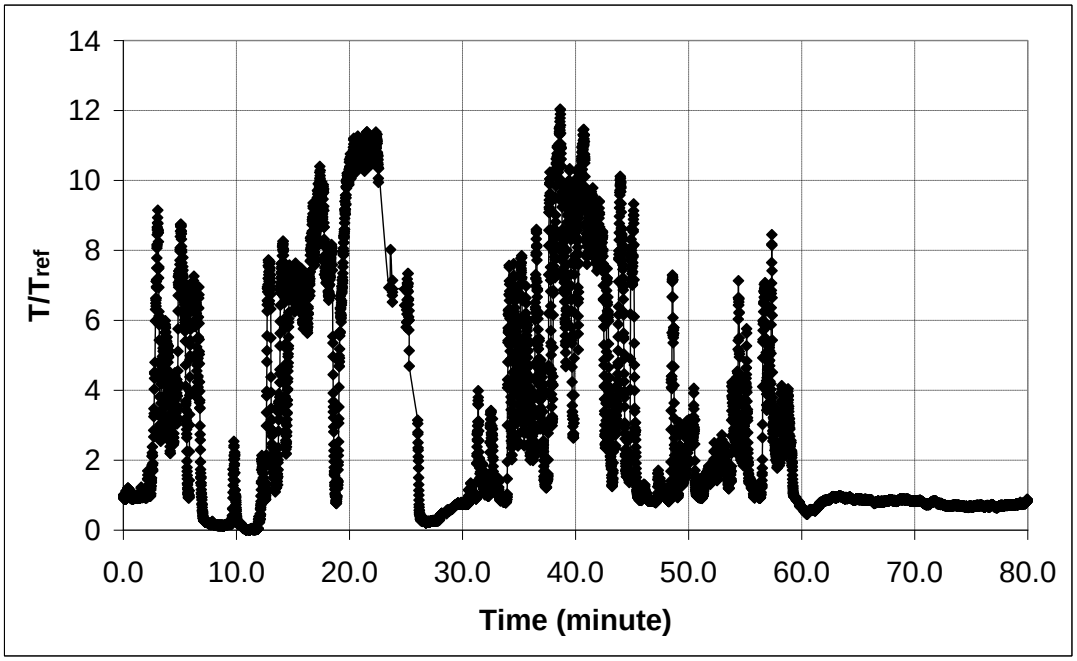

Figure 26 – Data collected at one thermocouple during the flight tests

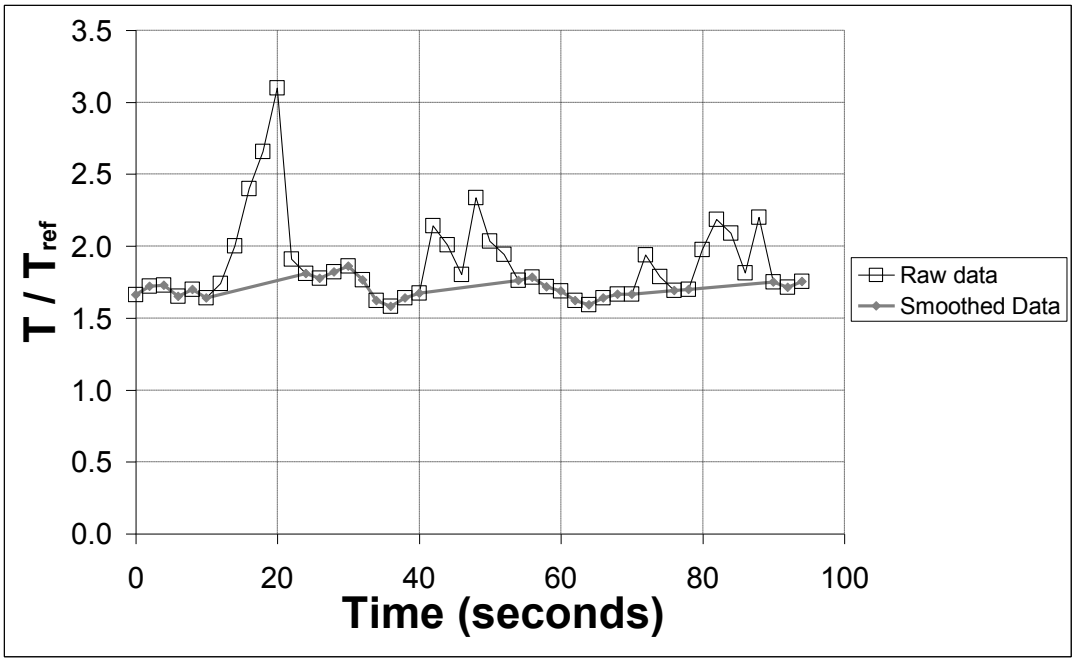

Figure 27 – Data collected at one thermocouple at one leg: raw data and smoothed data

4.2 MESH INDEPENDENCY

Before attempting to get meaningful comparisons between the measured data and the computed results, one must make sure the computed results are grid independent. For this, numerical solutions on the two grids whose properties were given in Section 3.2, which are basically different in size are obtained and compared for the advance ratio of 0.14 forward flight case.

Pressure coefficients extracted on the fuselage at the symmetry plane and at five longitudinal stations are plotted in Figure 28 to Figure 33. It is evident from the figures that the pressure coefficients for both solutions agree quite well.

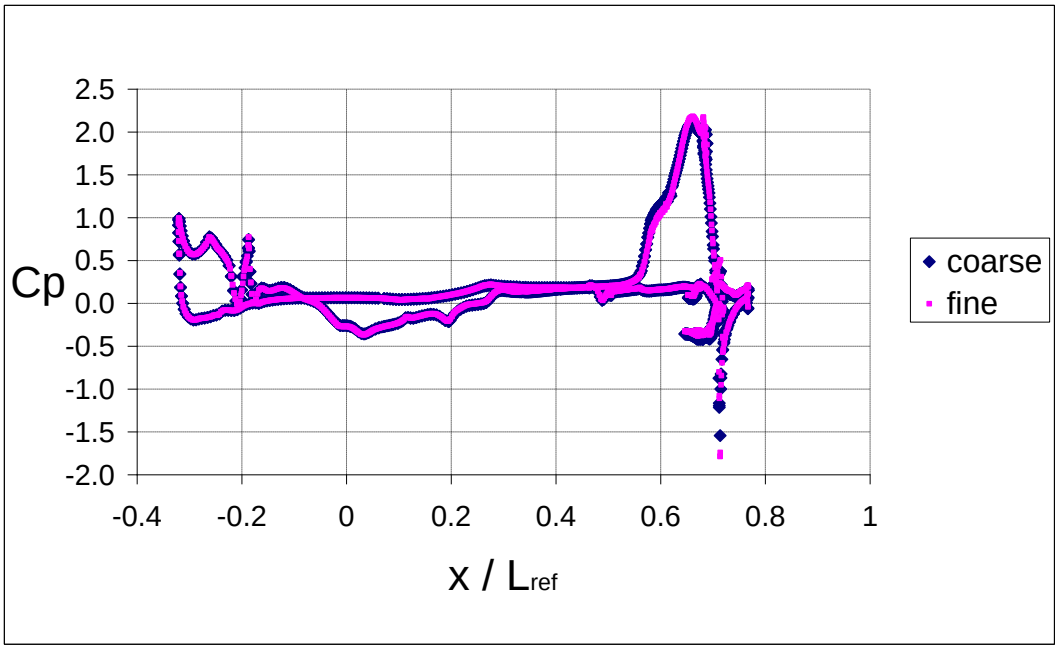

Figure 28 – Pressure coeffient on the fuselage at the symmetry plane obtained from coarse and fine grid solutions (μ=0.14)

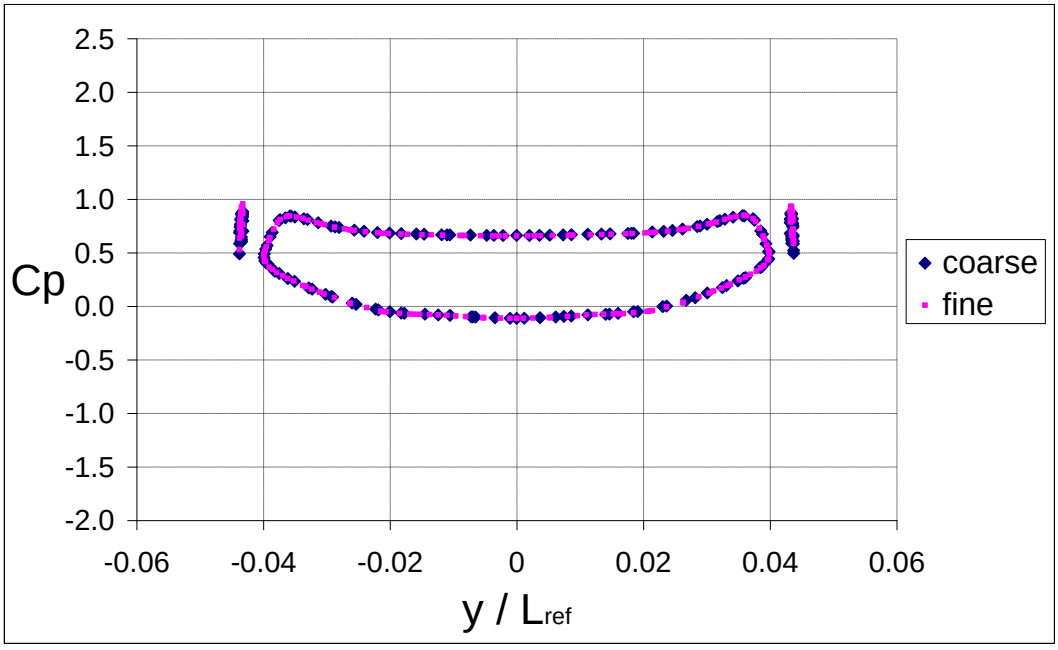

Figure 29 – Pressure coefficient on the fuselage at x/L_{ref}=-0.31 longitudinal station obtained from coarse and fine grid solutions (μ=0.14)

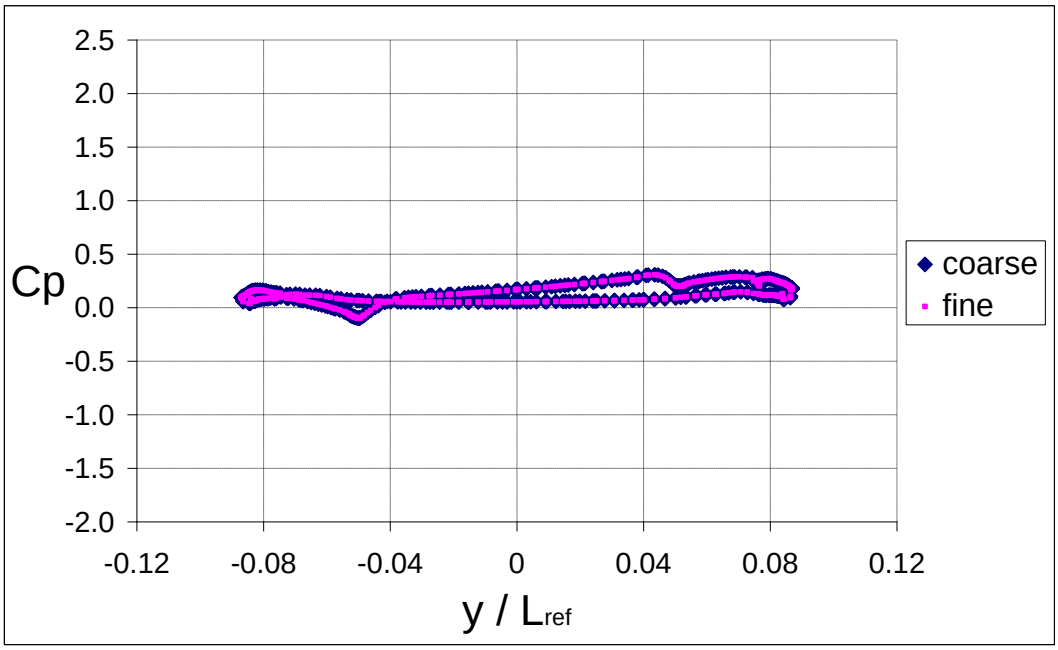

Figure 30 – Pressure coefficient on the fuselage at x/L_{ref}=-0.11 longitudinal station obtained from coarse and fine grid solutions (μ=0.14)

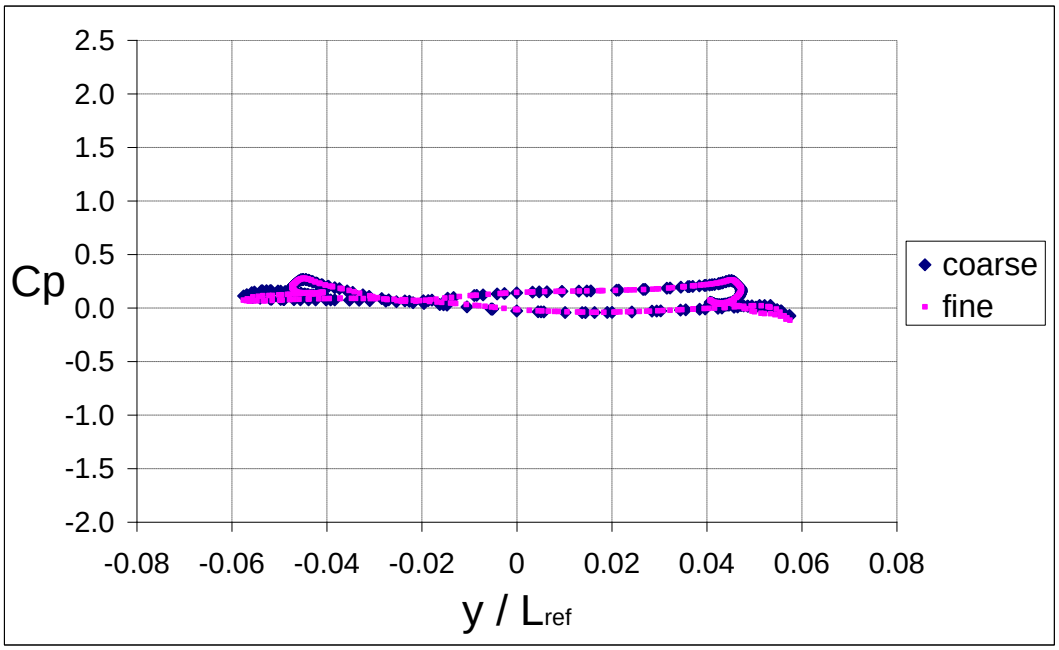

Figure 31 – Pressure coefficient on the fuselage at x/L_{ref}=0.23 longitudinal station obtained from coarse and fine grid solutions (μ=0.14)

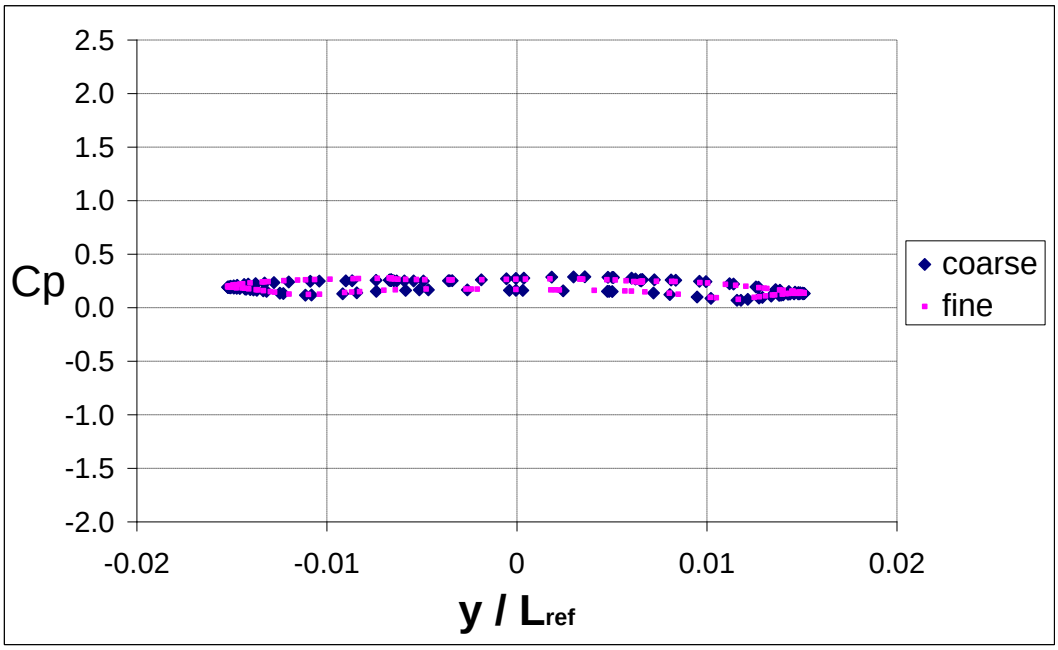

Figure 32 – Pressure coefficient on the fuselage at x/L_{ref}=0.55 longitudinal station obtained from coarse and fine grid solutions (μ=0.14)

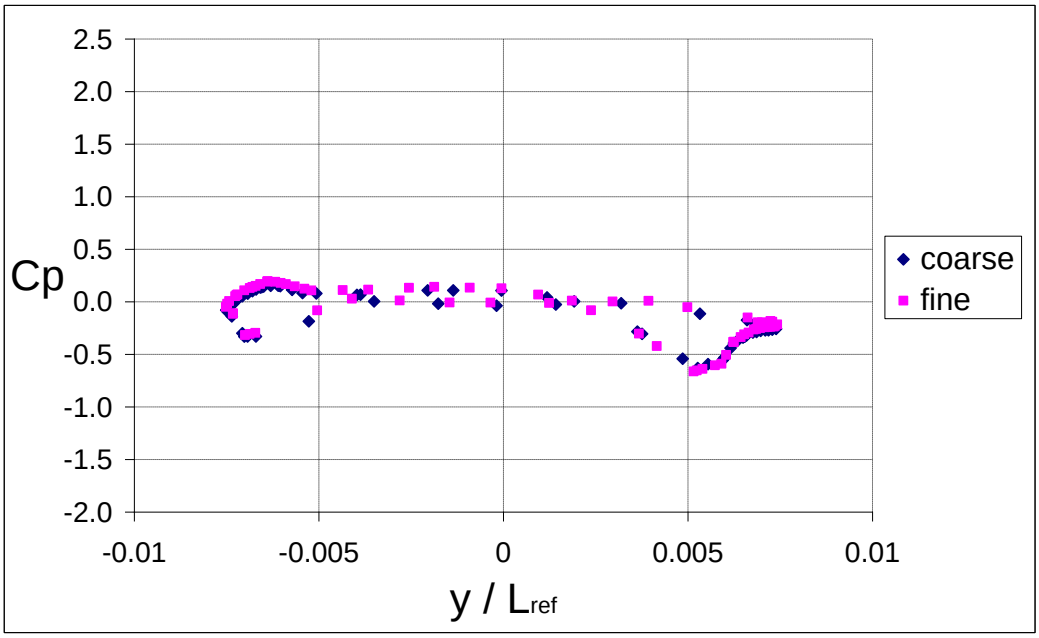

Figure 33 – Pressure coefficient on the fuselage at x/L_{ref}=0.75 longitudinal station obtained from coarse and fine grid solutions (μ=0.14)

The lift and drag coefficients and pitching moment coefficient for solutions are compared and given in Table 5.

Table 5 – Aerodynamic force and moment coefficients obtained from coarse and fine grid solutions (μ=0.14)

	MESH 1 (coarse)	MESH 2 (fine)	% Difference
C_D	0.2066	0.2046	1
C_L	0.114	0.113	0.9
C_{Mx}	0.0197	0.0196	0.6
C_{My}	-0.614	-0.620	0.8
C_{Mz}	0.0199	0.0197	0.8

A comparison for the temperature values are also made in Figure 61-Figure 64. In these figures good agreement is also observed for the temperature values.

In the light of these results, it is now more important to compare the computational efforts spent on these meshes. It was found that the computational time required for one iteration on the fine mesh was about 2.3 times longer than the time it took on the coarse mesh configuration in terms of wall-clock time. Therefore, it was concluded that the coarse mesh could be used for the rest of the analyses.

In the sections below, the forward flight results will be given and discussed first. As aforementioned, the forward flight results were obtained at four different advance ratios. These were 0.07, 0.14, 0.19, and 0.28, respectively. The temperature results are compared to available flight test results. At this point it will be useful to note that in the computations, the fuselage and tip path plane angles for each

computation were set according to the flight velocity (advance ratio). These values were obtained from the study of Caliskan [16].

4.3 FORWARD FLIGHT AT μ=0.28

Advance ratio of 0.28 represents a reasonably high flight velocity. Therefore, at μ=0.28, the effect of the forward flight velocity is clearly observed. Figure 34 and Figure 35 show some streamlines trailing the main rotor. The rotor wake appears to be dragged downstream, washing the rear parts of the fuselage, interacting with the vertical and horizontal tails and the tail rotor (Figure 36).

During the flight tests two different stores were mounted upstream of the tail boom on left and right sides. The flow meeting the stores was deflected upwards into the exhaust jet. Therefore, the wakes of the stores were heated up before they hit the tail boom and thereby increasing the temperature of the upper part of the boom further. These stores were also included in the computations.

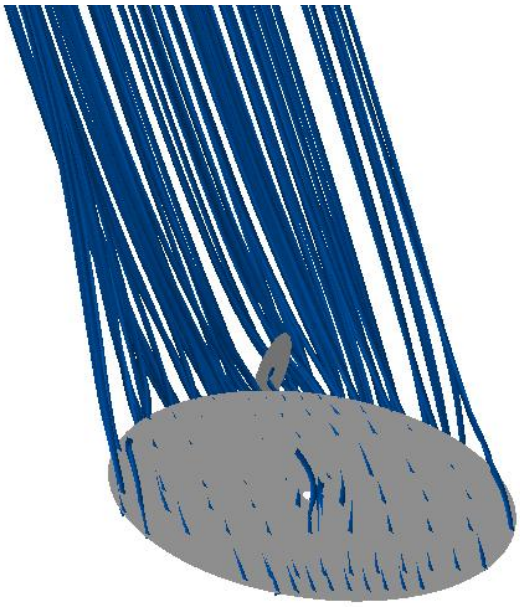

Figure 34 – Main rotor streamlines at μ=0.28

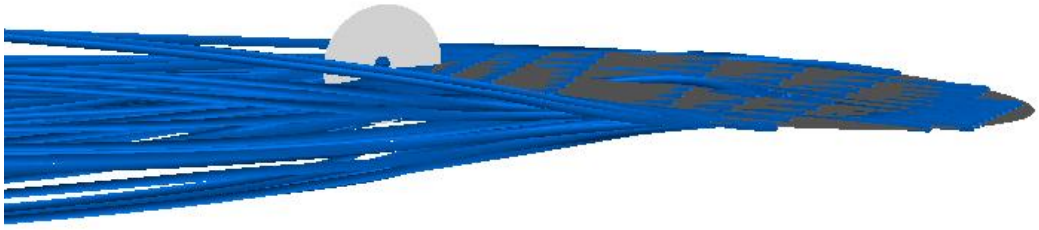

Figure 35 – Main rotor streamlines at μ=0.28 - side view

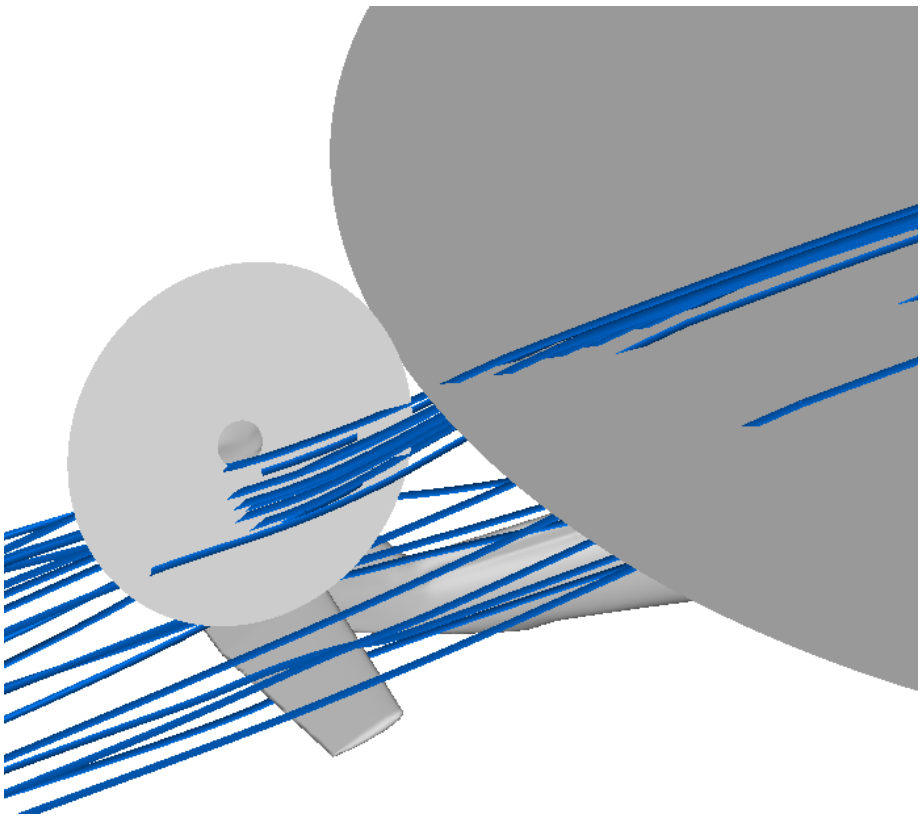

Figure 36 – Main rotor - tail rotor, main rotor –vertical and horizontal tail interactions at μ=0.28

The rotor wake interacted with the exhaust gases such that the paths of the hot gases from the left and the right exhausts are different. On the right side, the exhaust comes closer to the tail boom heating that region more than the left side as can be observed in Figure 37. Due to the high forward flight velocity, the rotor downwash is not as effective as it would be at a low speed flight in pushing the hot flow downward. Therefore, the rear upper region of the tail is affected mainly by the hot flow.

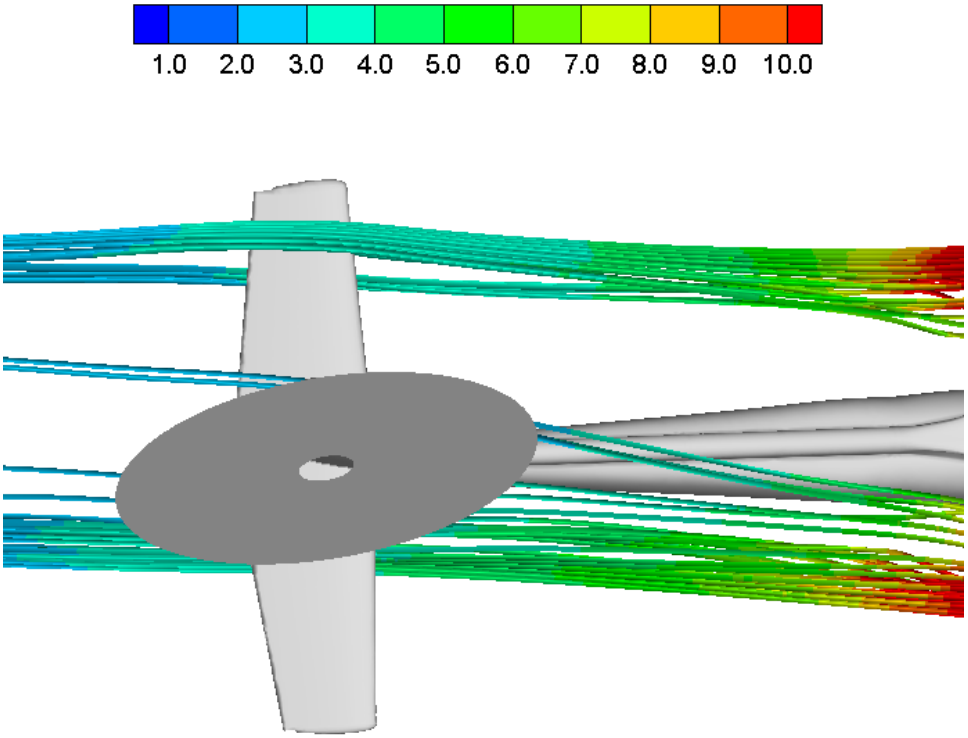

Figure 37 – Exhaust streamlines at μ=0.28 (colored by temperature: T/T_{ref})

The temperature iso-surfaces shown in Figure 38 also demonstrate how the exhaust jet gets diffused and convected as well as the effects of the store wakes. These effects are quantified by the contour plots presented in Figure 39 and Figure

40. Due to high forward flight velocity the lower regions of the tail boom seem to get heated slightly by the exhaust jet.

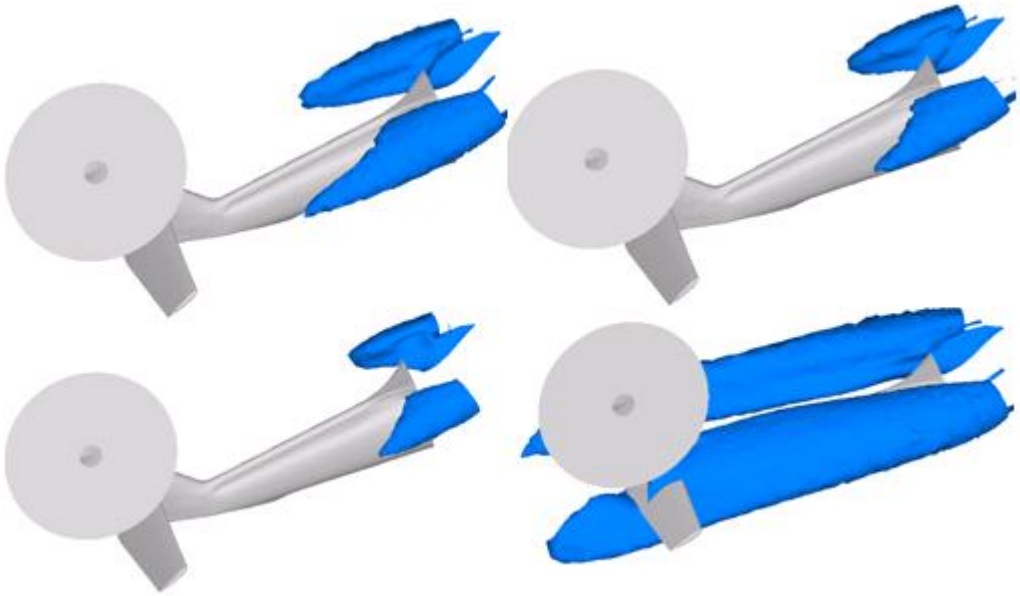

Figure 38 – Temperature iso-surfaces at μ=0.28

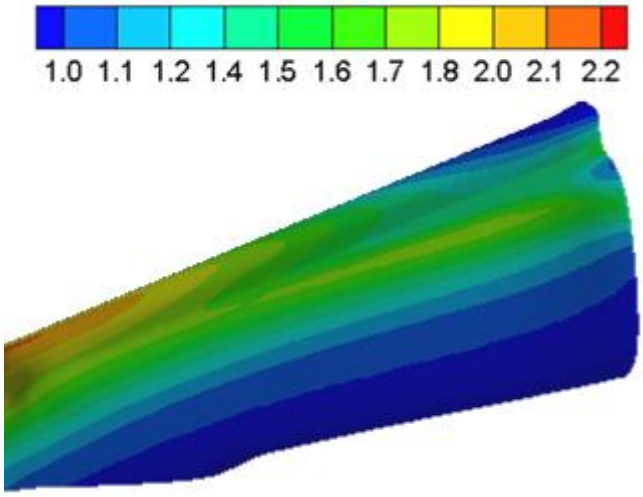

Figure 39 – Temperature distribution on the tail boom at μ=0.28- right side

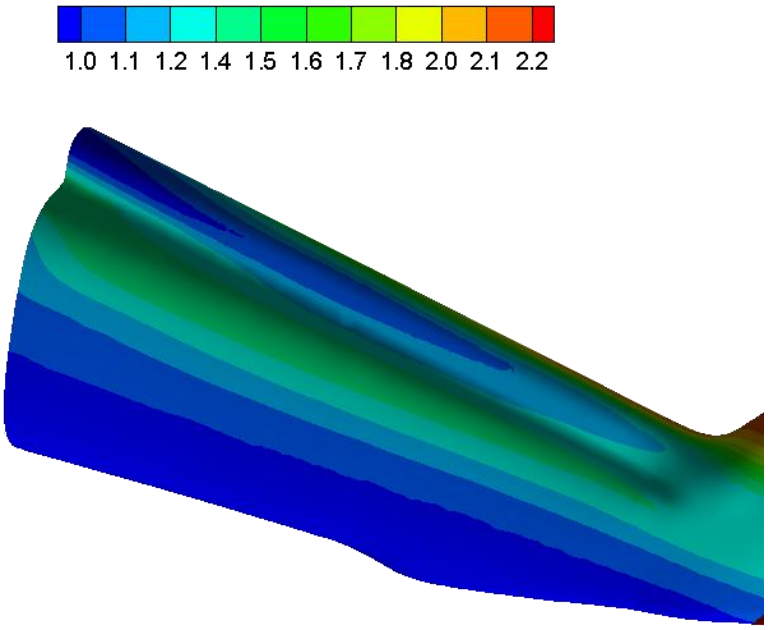

Figure 40 – Temperature distribution on the tail boom at μ=0.28- left side

The temperature values around the tail boom are compared to that obtained from the flight tests. Scales of the temperature axes are adjusted to have the identical range for all four graphs. The exhaust location is x/L_{ref}= 0.21. It is evident from Figure 41 that the trends agree with those of the flight test data on the right upper side. On this side the values are slightly overestimated but still close to the test data. The increase in temperature after about x/L_{ref}=0.32 caused mainly by the effect of the store wake was overpredicted by the CFD solution. The non-constant difference in temperature is considered natural since the jet experiences a diffusion process. Therefore, different points get influenced differently by the exhaust jet. Moreover, the wake of the stores interact with the exhaust jet. On the lower right side, the temperature remains close to the free-stream temperature upstream of the x/L_{ref}=0.47 location for both the test data and the CFD solution (Figure 42). Only downstream of the x/L_{ref}=0.47 position has increasing temperature. Hot spots on tail were predicted by the numerical solution quite well. However, the temperature values there were somewhat underpredicted.

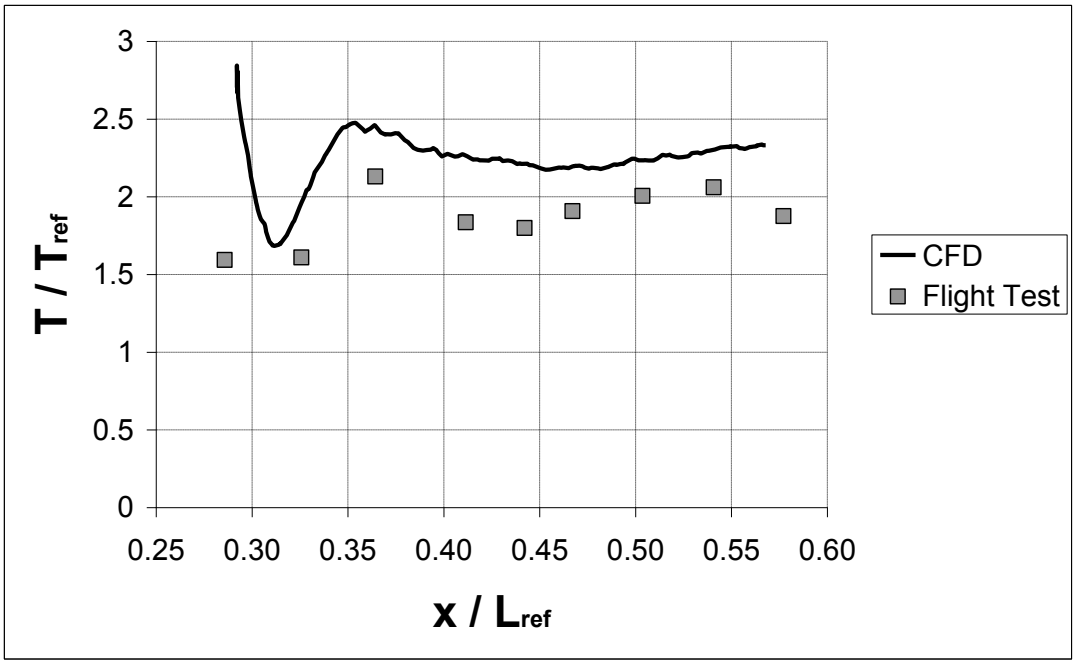

Figure 41 – Temperature values on the upper right data line at μ=0.28

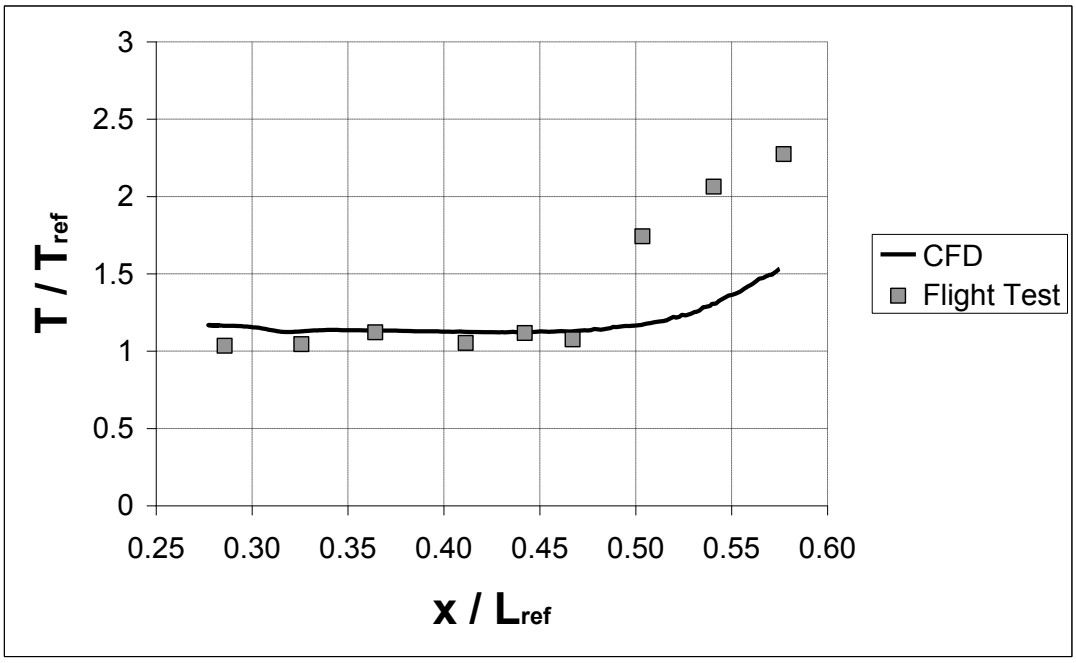

Figure 42 – Temperature values on the lower right data line at μ=0.28

On the upper left side the numerical solution overestimated the temperature distribution as can be noticed in Figure 43. The upper left side is influenced by the store wake. The flight test, as well, demonstrated the heating caused by the stores localized about x/L_{ref}=0.4. Flight test data showed that, the lower left side was not heated. CFD simulation gave a similar result (Figure 44).

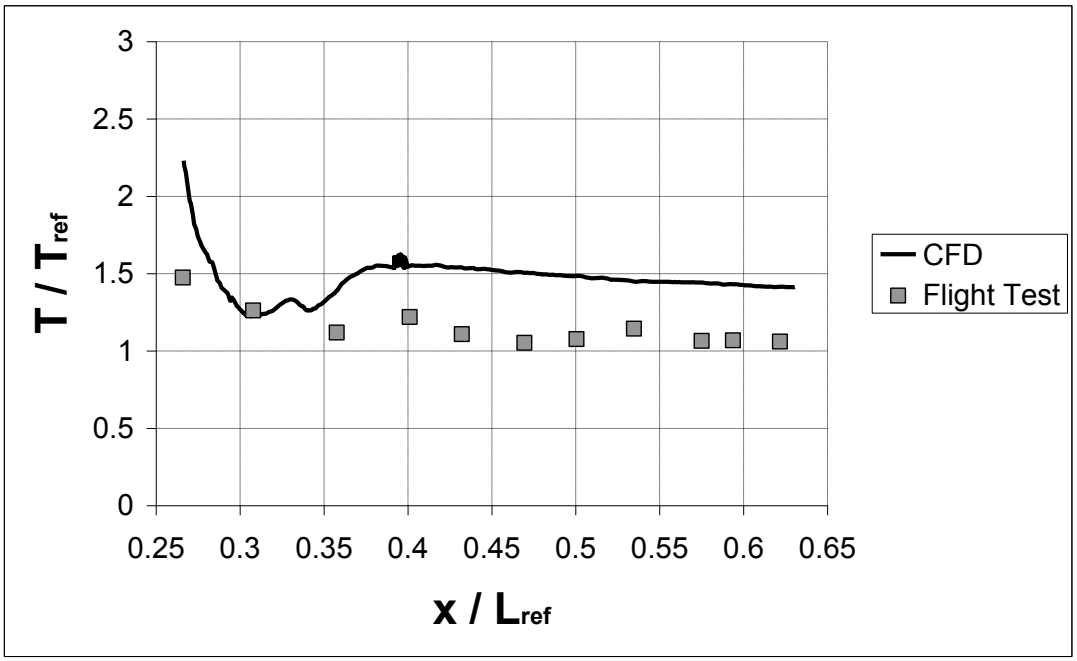

Figure 43 – Temperature values on the upper left data line at μ=0.28

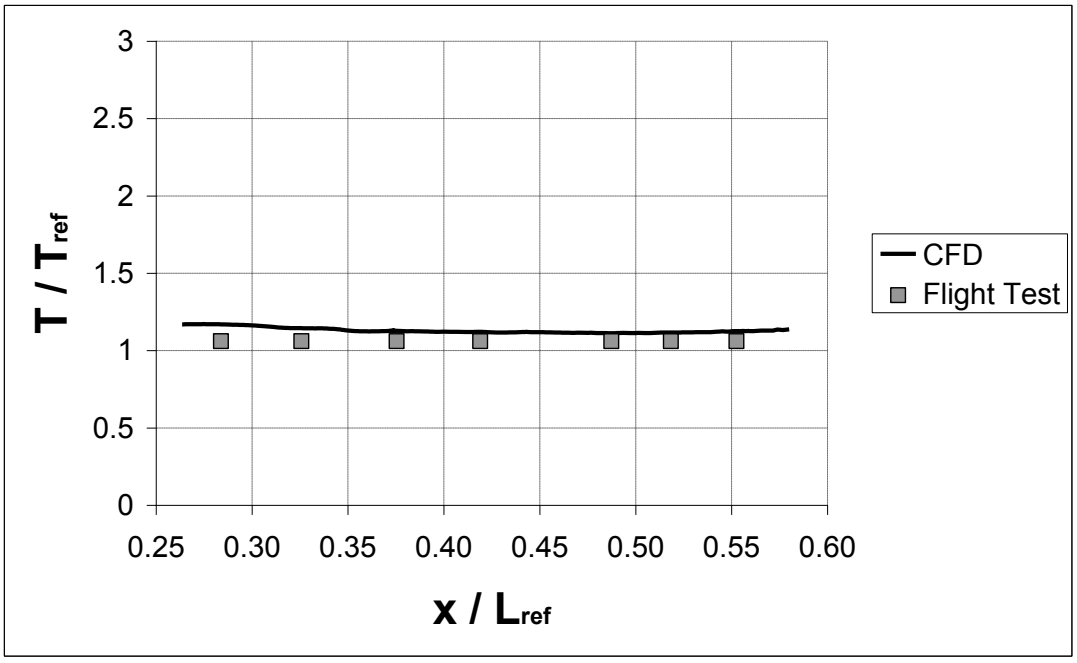

Figure 44 – Temperature values on the lower left data line at μ=0.28

As a whole, the CFD simulation could capture the general behavior of the flow reasonably well, though it overestimated the local temperature values in some parts. One possible reason for the overestimation is the assumption of uniform temperature distribution on the exhaust face. Another reason can be attributed to the possibility on atmospheric disturbances. There is no detailed record of the atmospheric conditions for the duration of the data acquisition. In addition, the store details were neglected, although it was very rough.

4.4 FORWARD FLIGHT AT μ=0.19

Just like the previous case, at μ=0.19, the rotor wake sheds downstream due to the forward flight velocity. Formation of the tip vortices can easily be observed in Figure 45-Figure 46.

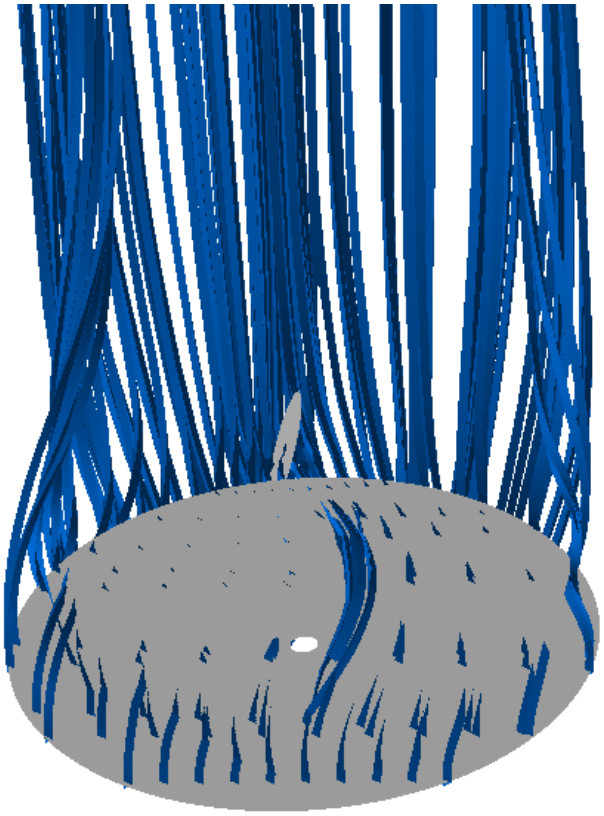

Figure 45 – Main rotor streamlines at μ=0.19

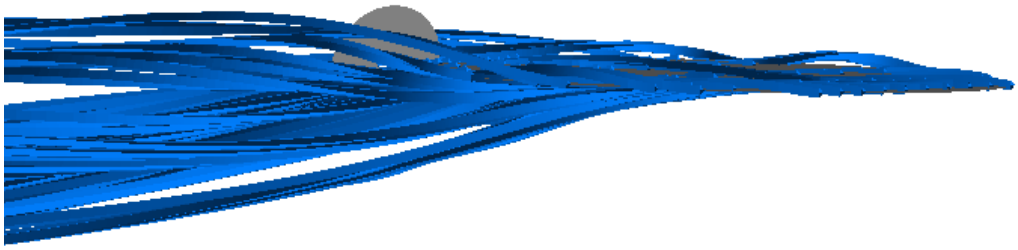

Figure 46 – Main rotor streamlines at μ=0.19- side view

As in the μ=0.28 case, the exhaust jets do not seem to follow symmetric paths; rather, the right jet is somewhat deflected toward the fuselage and jumps to the left side of it. The stores contributed to this jump. This causes an interaction of the

flows on the two sides of the airframe. The streamlines released from the exhaust and temperature iso-surfaces show this interaction (Figure 47-Figure 48).

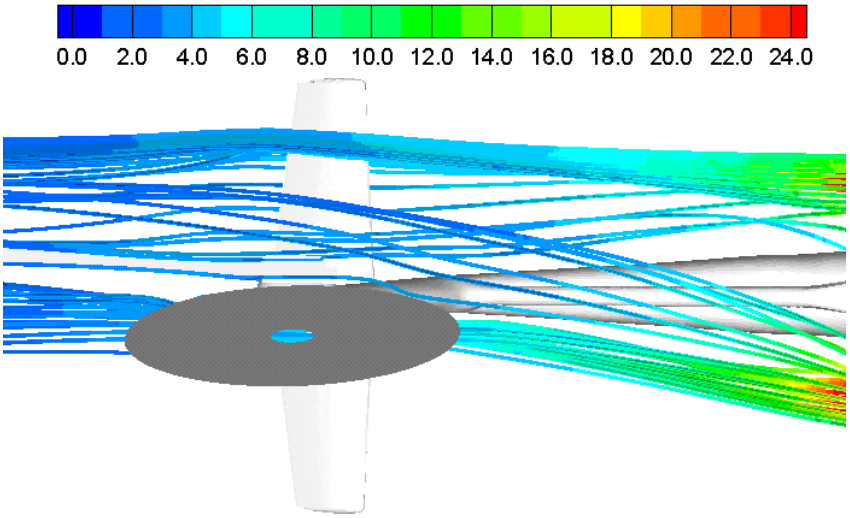

Figure 47 – Exhaust streamlines at μ=0.19 (colored by temperature: T/T_{ref})

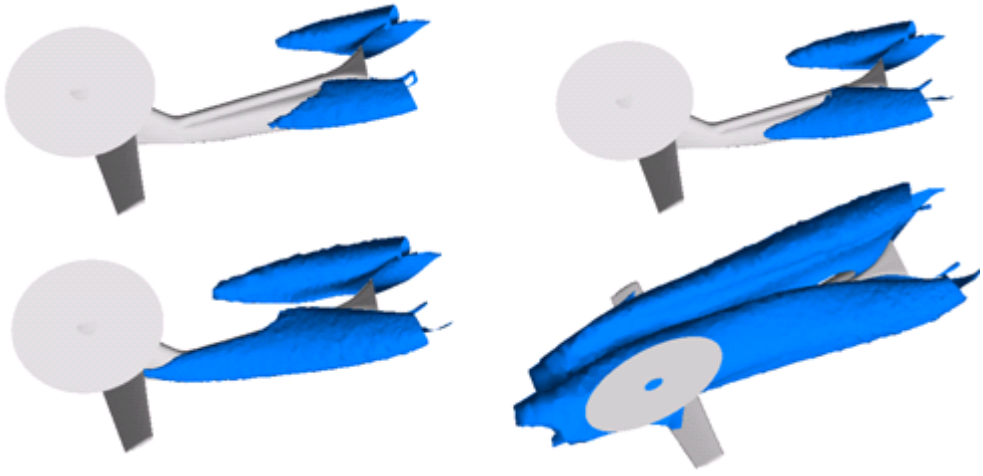

Figure 48 – Temperature iso-surfaces at μ=0.19

The heated regions of the tail boom seem to move downward as compared to the μ=0.28 case, since the forward flight velocity is lower and the rotor downwash is more effective in this case (Figure 49-Figure 50).

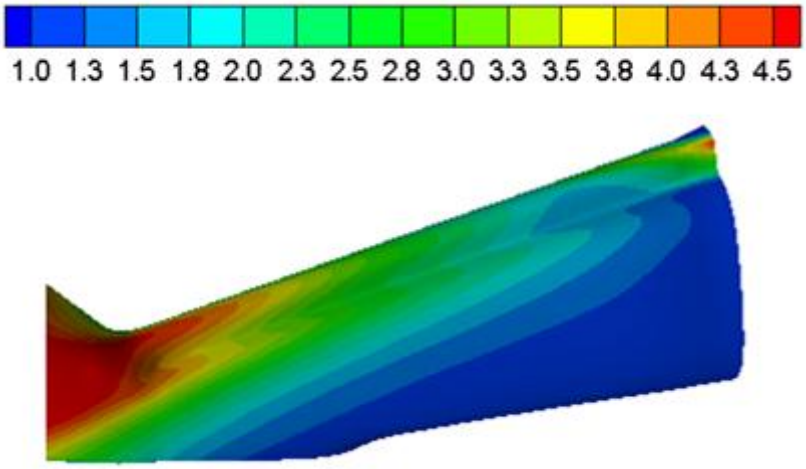

Figure 49 – Temperature distribution on the tail boom at μ=0.19- right side

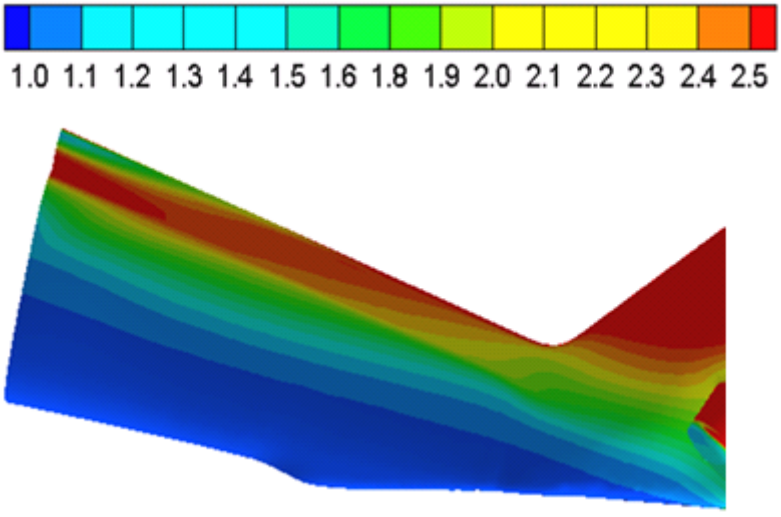

Figure 50 – Temperature distribution on the tail boom at μ=0.19- left side

As in the μ=0.28 case, the temperature distributions around the tail boom shows similar trends to those of the flight test data with some overpredicted values.

On the upper right side (Figure 51) the temperature difference between the flight test data and the CFD solution increased downstream of the location where the exhaust jet and store wake were closest to the fuselage and jumped to the left side. This was a similar situation to the μ=0.28 case although the increase around the x/L_{ref}=0.33 position was predicted better. The temperatures were overpredicted on the upper left side (Figure 53) where the store wake was quite influential, whereas the lower right and left sides showed very good agreement with the test data (Figure 52-Figure 54)

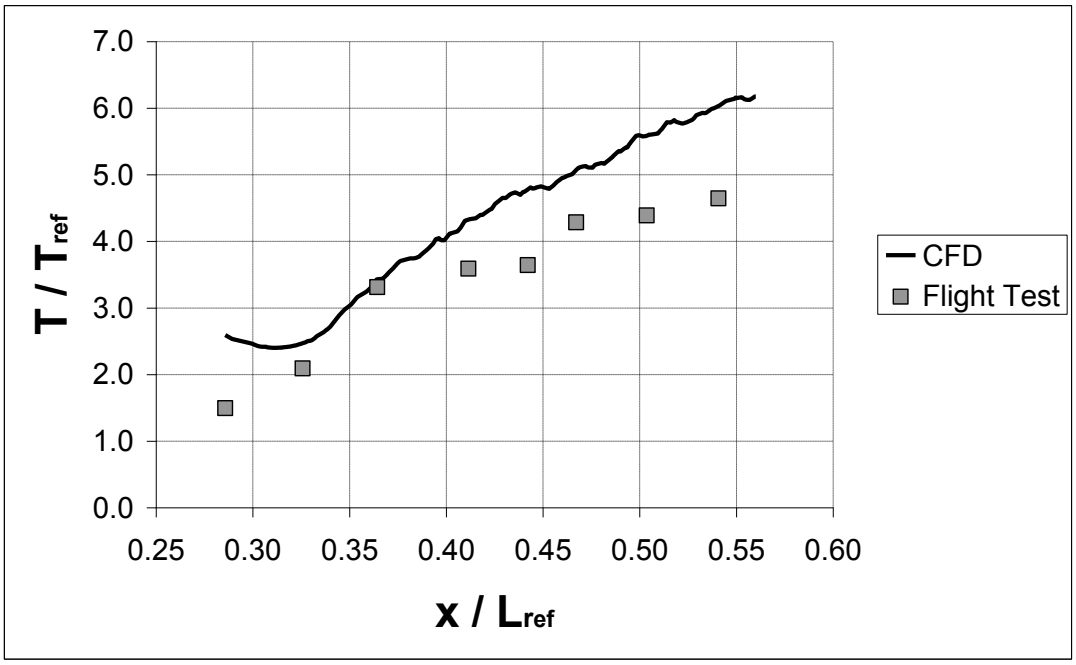

Figure 51 – Temperature values on the upper right data line at μ=0.19

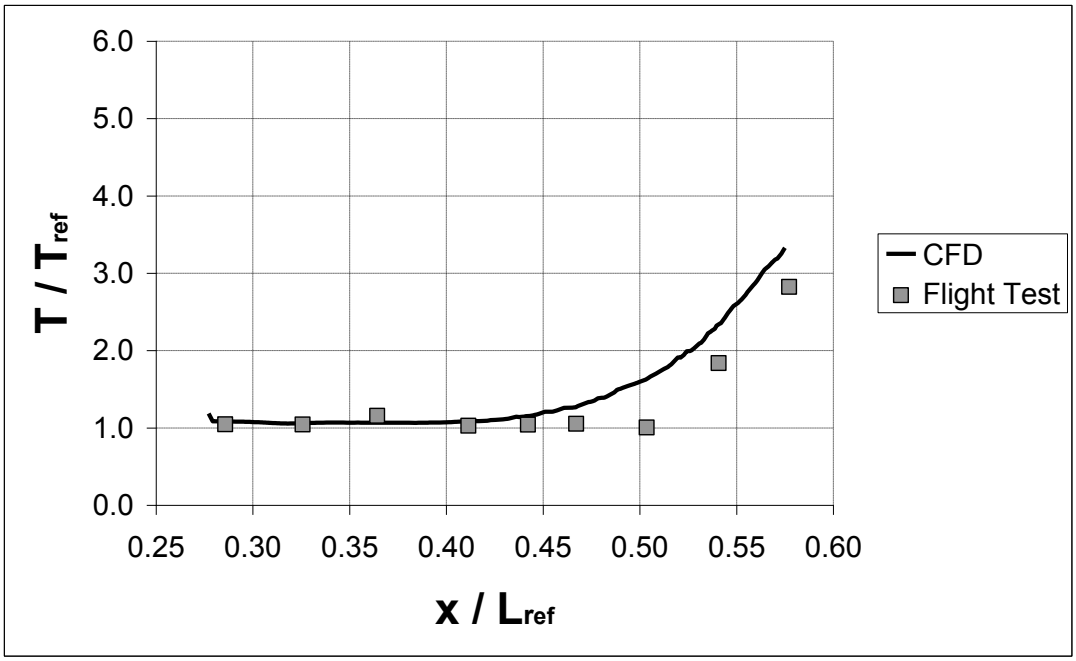

Figure 52 – Temperature values on the lower right data line at μ=0.19

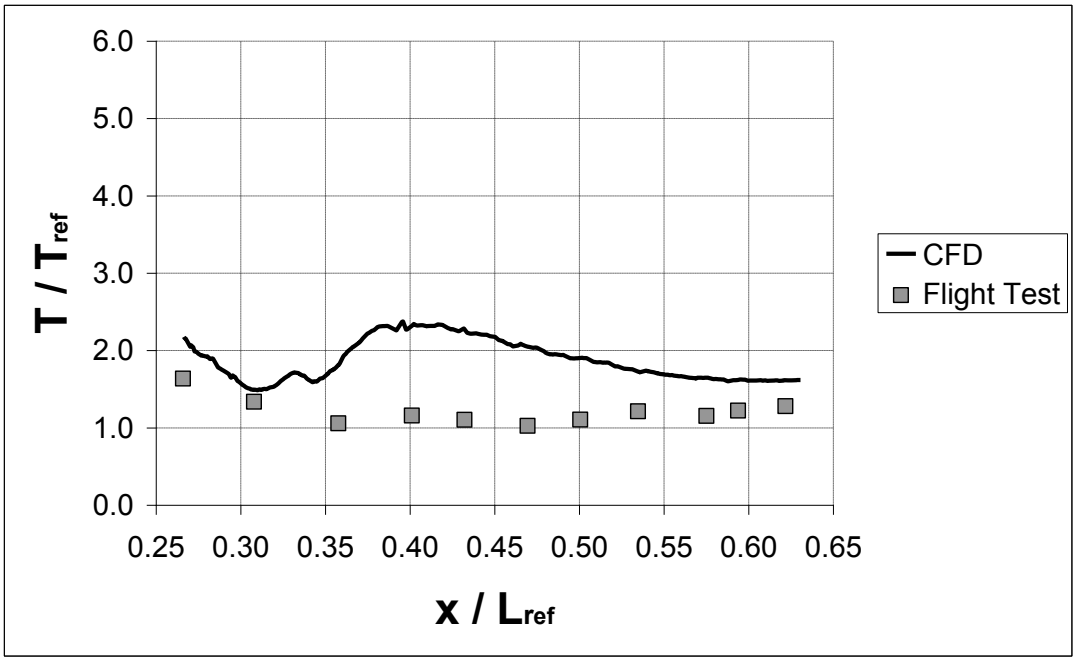

Figure 53 – Temperature values on the upper left data line at μ=0.19

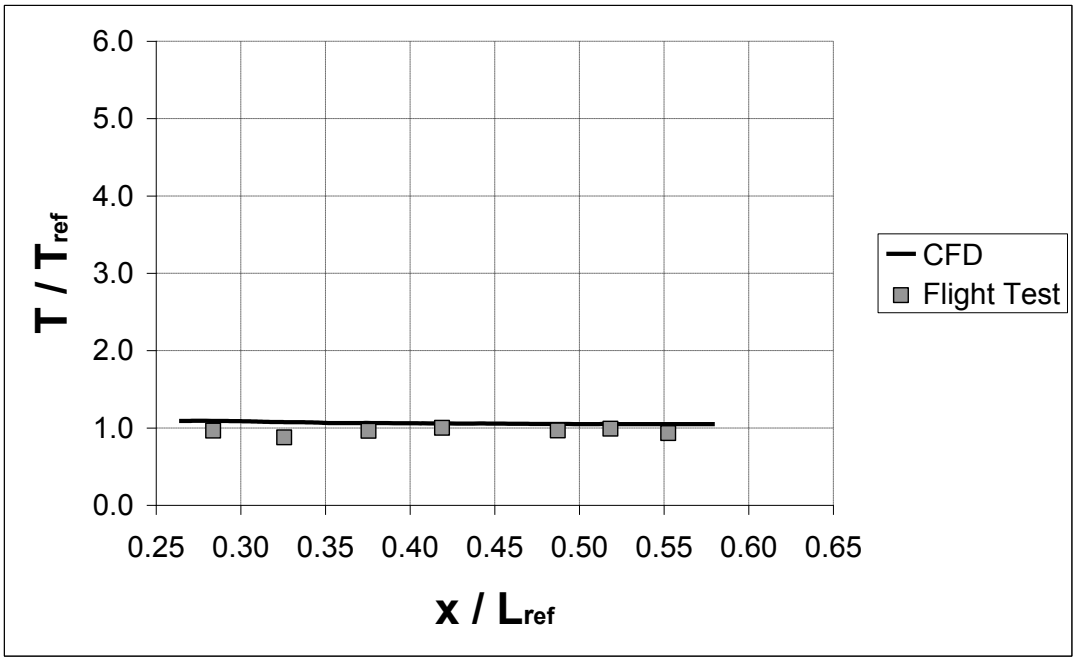

Figure 54 – Temperature values on the lower left data line at μ=0.19

4.5 FORWARD FLIGHT AT μ=0.14

For this case Figure 55 and Figure 56 show that the rotor wake shed downward more than the previous cases as a result of the reduced forward velocity. From the figures the vortical structure of the wake is quite evident. Also, the right exhaust jet passed to the left side as it did in μ=0.19 case. The streamlines released from the exhaust are given in Figure 57.

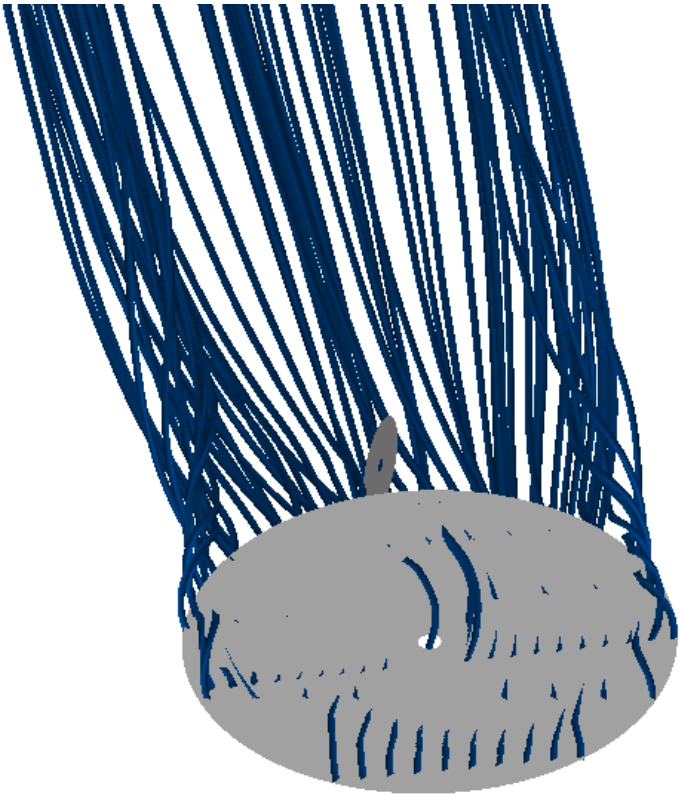

Figure 55 – Main rotor streamlines at μ=0.14

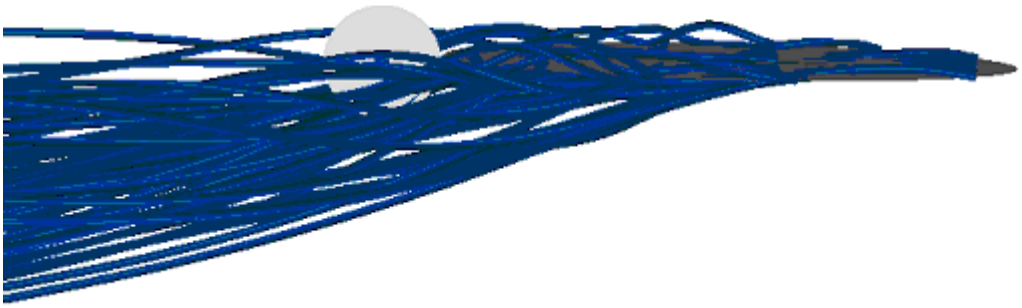

Figure 56 – Main rotor streamlines at μ=0.14 - side view

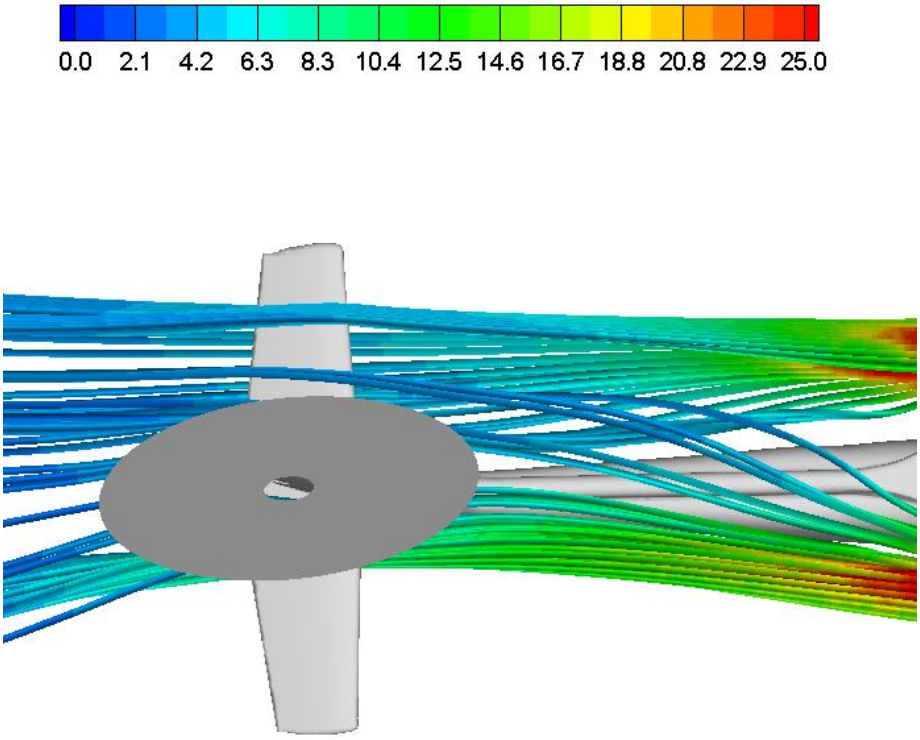

Figure 57 – Exhaust streamlines at μ=0.14 (colored by temperature: T/T_{ref})

The development of the hot flow region can be seen from the temperature iso-surfaces as well which are given Figure 58. The temperature distribution shows that the rotor wake is even more effective than the μ=0.19 and μ=0.28 cases, as expected, since the area affected by the hot region extends to the downward parts of the tail boom as evident in Figure 59 and Figure 60.

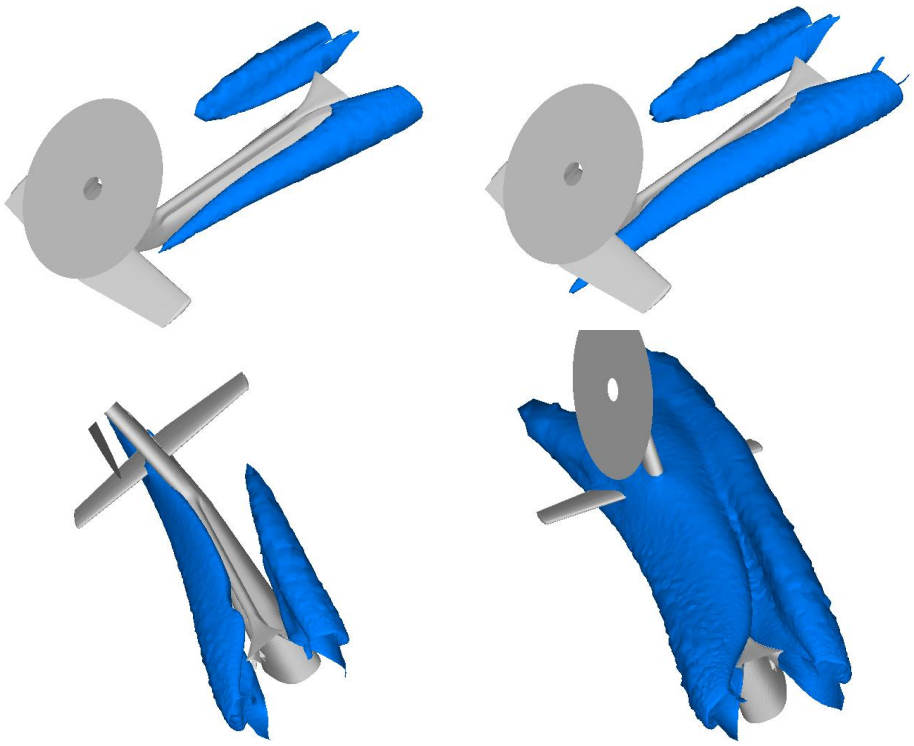

Figure 58 – Temperature iso-surfaces at μ=0.14

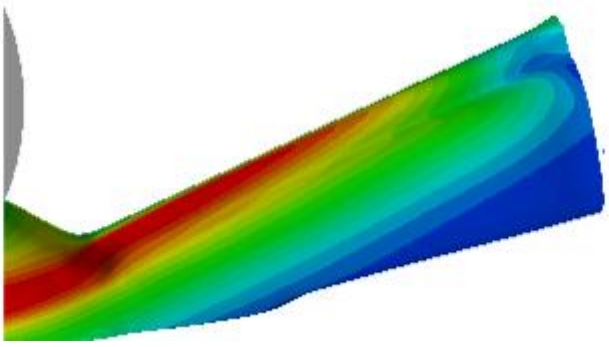

Figure 59 – Temperature distribution on the tail boom at μ=0.14- right side

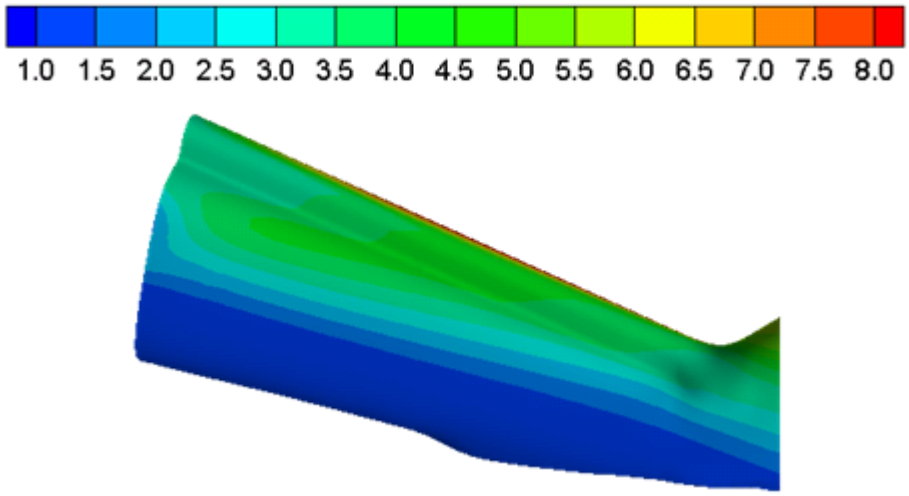

Figure 60 – Temperature distribution on the tail boom at μ=0.14- left side

The trend of the temperature distribution obtained from the CFD simulation on the upper right side resembles the flight test data as shown in Figure 61. However, the values diverge from the test measurements past the x/ L_{ref}= 0.37 station. Upstream of this location the hot flow shedding on the right side starts to pass to the left side heating up the upper part of tail from that point on. The temperature in this region is overestimated; a situation similar to the other cases discussed. Likewise, the lower right side trend was captured quite well by the numerical analysis (Figure 62). However, the flight test data showed that the temperature starts to rise at locations further downstream.

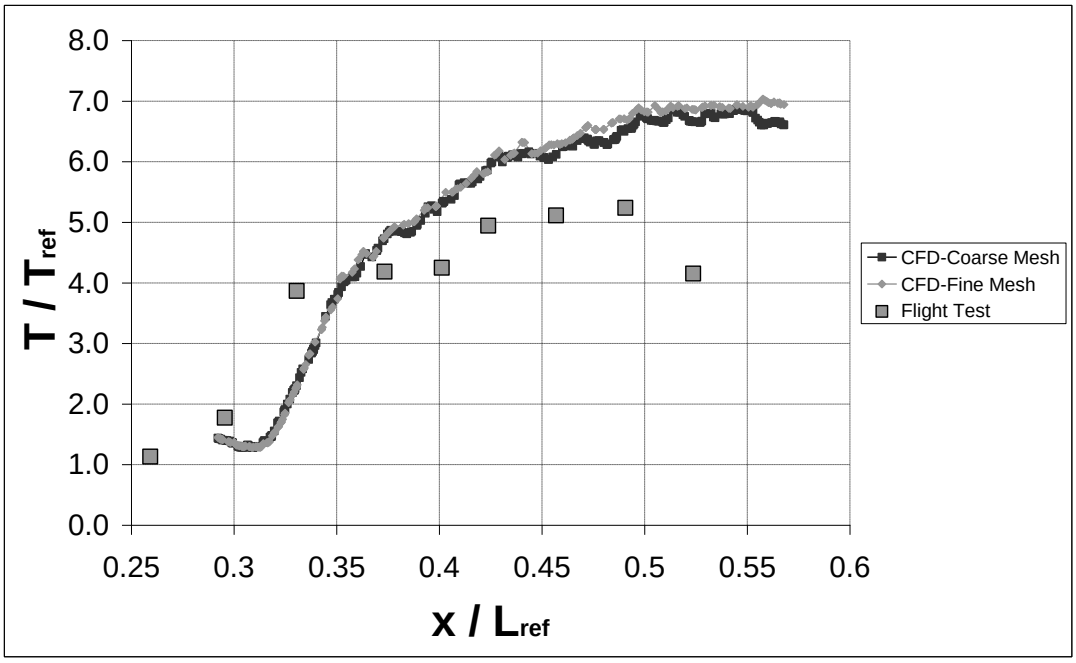

Figure 61 – Temperature values on the upper right data line at μ=0.14

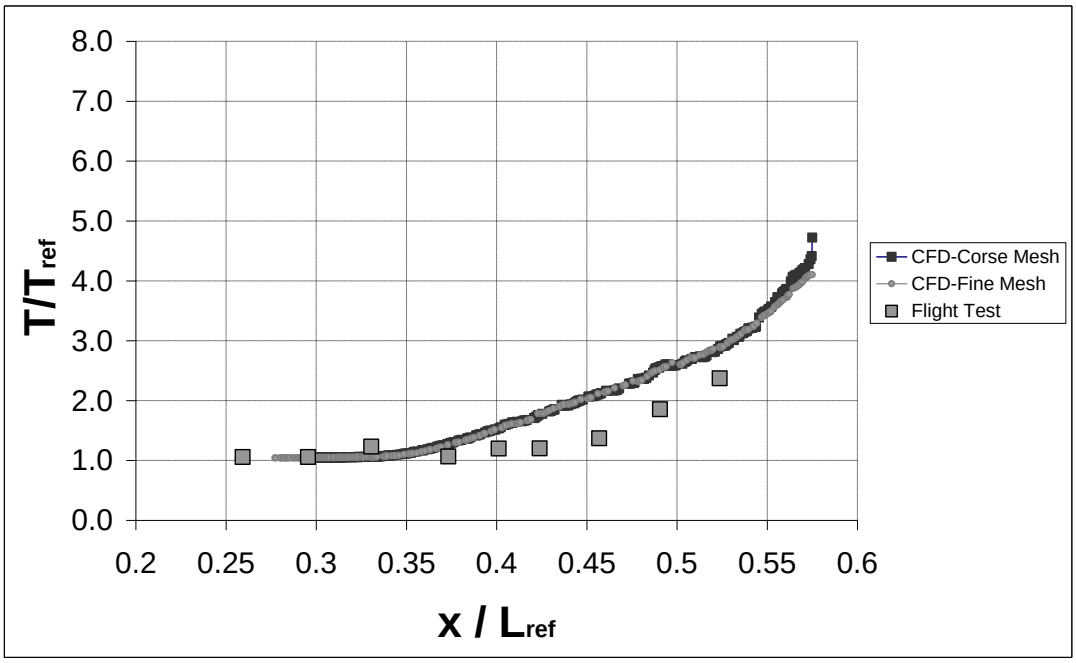

Figure 62 – Temperature values on the lower right data line at μ=0.14

Figure 63 shows the upper left side comparison. It is clear from the figure that while the test data remains close to the free-stream values at all stations, the simulation shows that the tail boom is heated there to higher temperatures. The effect of the hot flow did not spread to the lower left side, however as clear from Figure 64. This again shows that the wake of the stores has some influence on the temperature distribution. Therefore, it can be stated that the flow features that result from the presence of the stores were not captured well by the simulation.

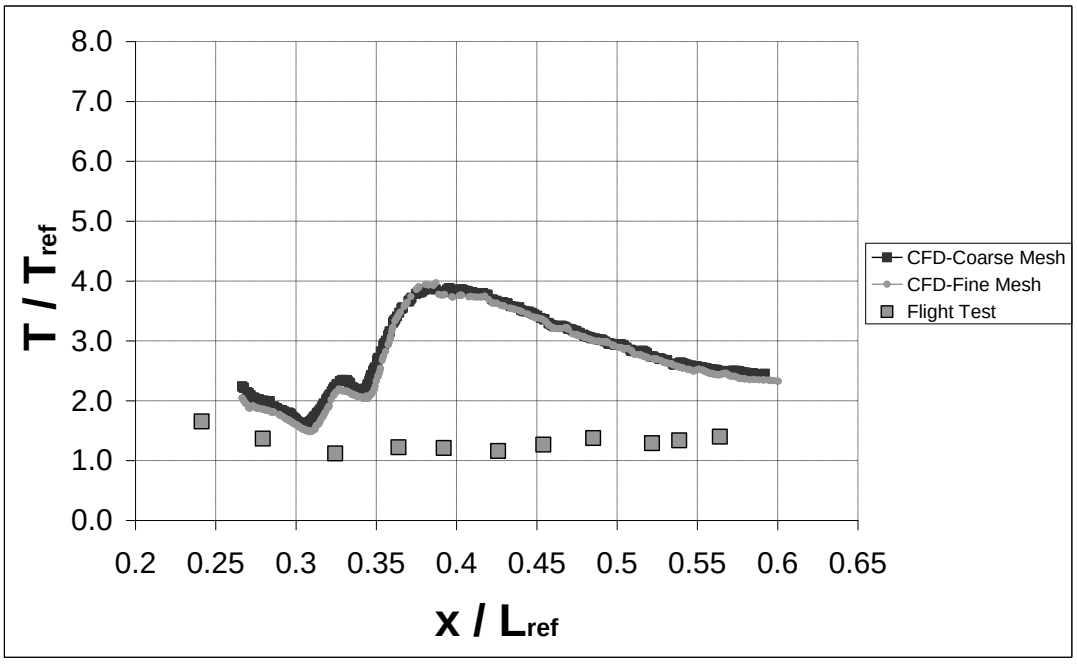

Figure 63 – Temperature values on the upper left data line at μ=0.14

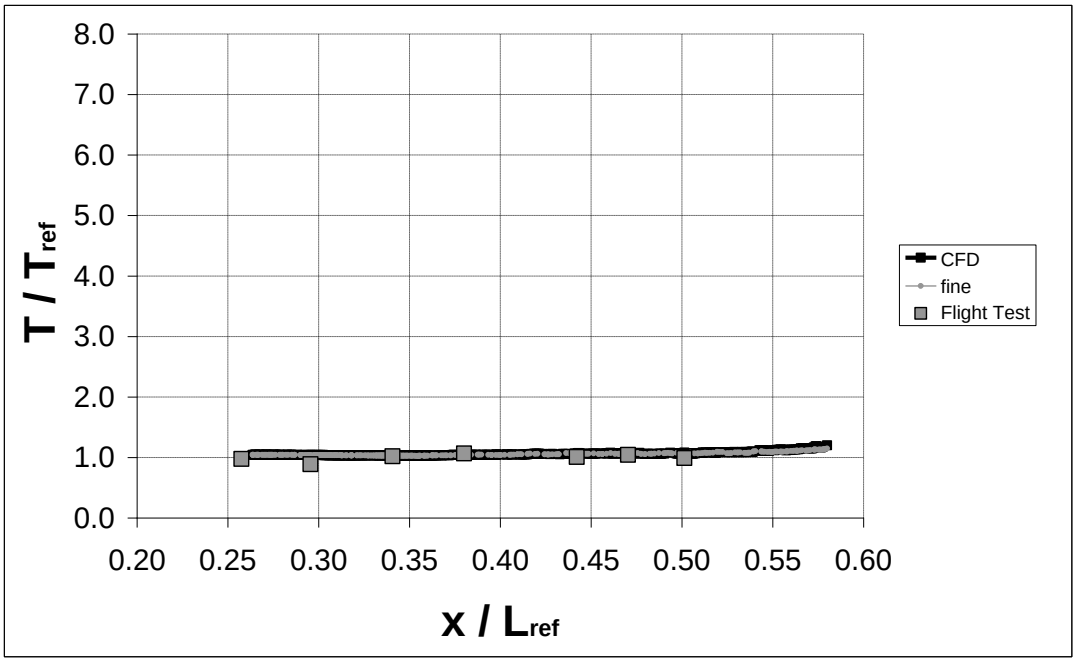

Figure 64 – Temperature values on the lower left data line at μ=0.14

4.6 FORWARD FLIGHT AT μ=0.07

Flight at μ=0.07 was a low speed flight demonstrating the domination of the rotor wake in the flow field as evident from the rotor wake structure shown in Figure 65 and Figure 66. The tip vortices seem stronger and more apparent. The flow is pushed down towards the fuselage more strongly as it also sheds downstream with the effect of the forward flight velocity. The rotor downwash has a remarkable influence on the exhaust jet pushing it downward, thereby forcing it to heat the upstream parts of the tail boom only as illustrated in Figure 67 and Figure 68. At this advance ratio, the left exhaust comes closer to the fuselage than the right one.

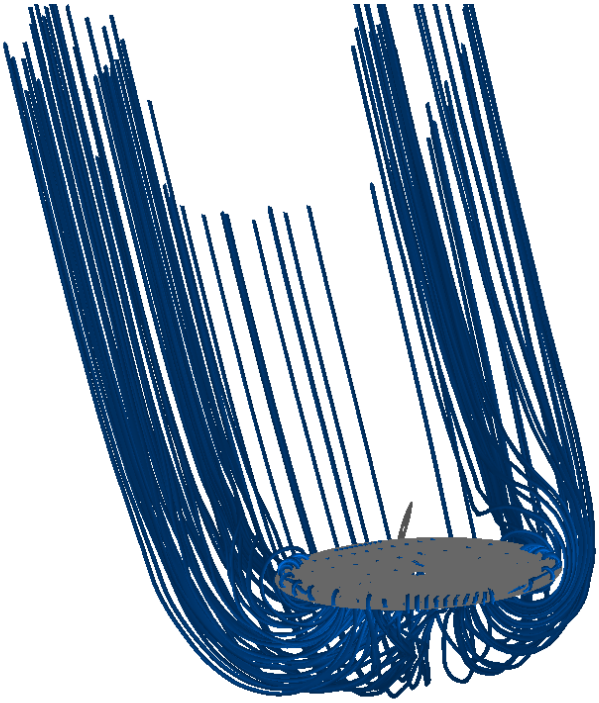

Figure 65 – Main rotor streamlines at μ=0.07

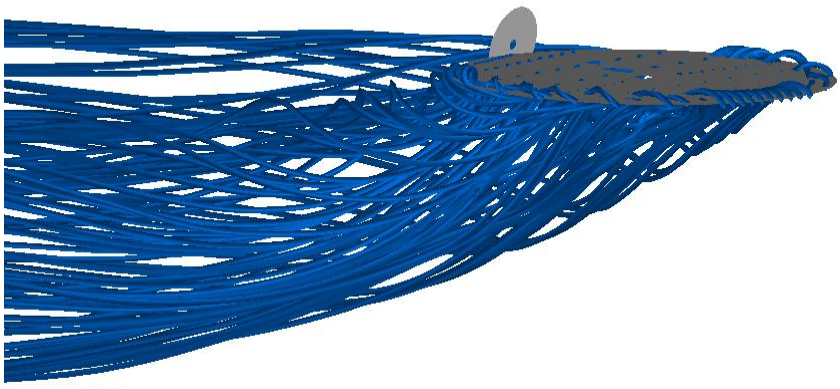

Figure 66 – Main rotor streamlines at μ=0.28 - perspective

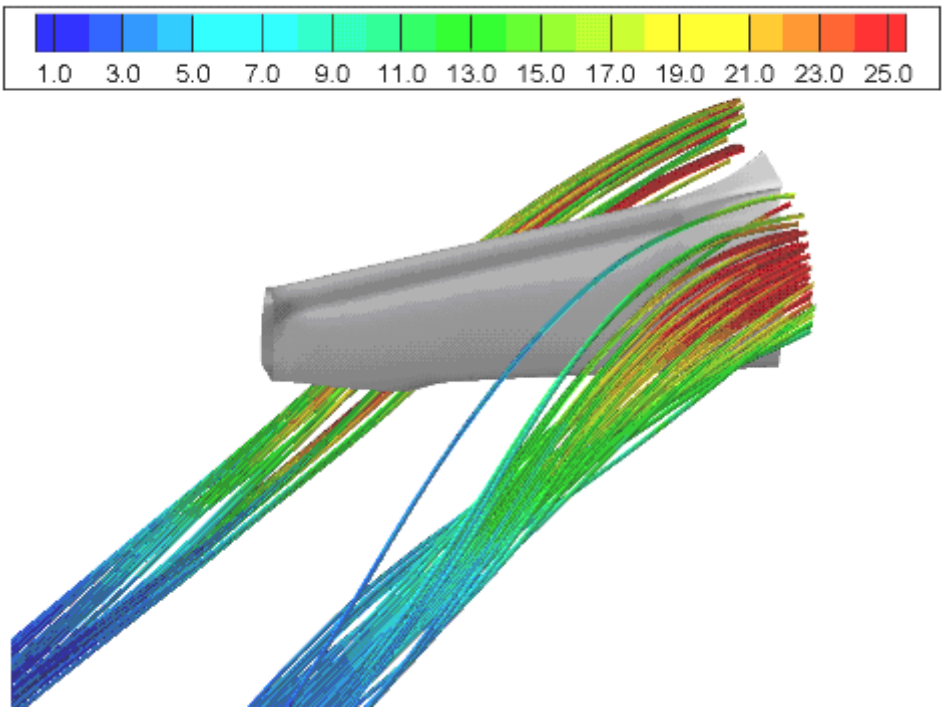

Figure 67 – Exhaust streamlines at μ=0.07 (colored by temperature: T/T_{ref})

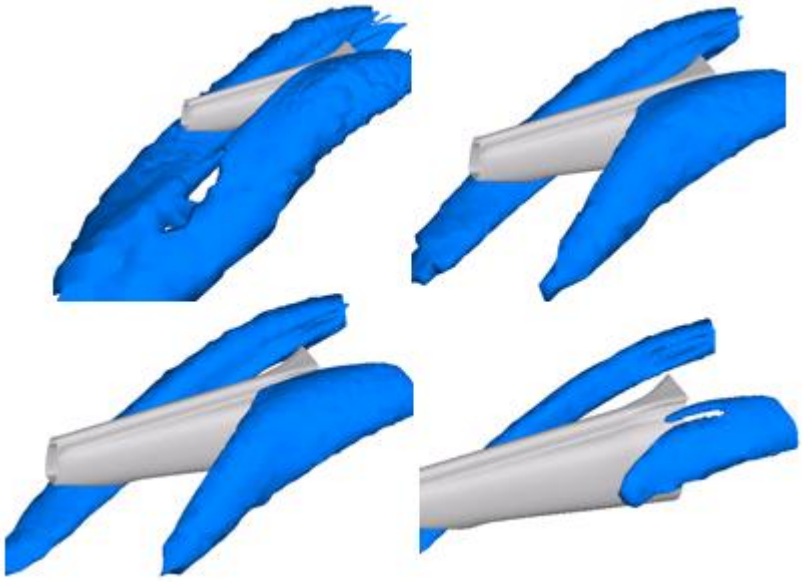

Figure 68 – Temperature iso-surfaces at μ=0.07

The temperature distributions reveal the effect of the rotor wake. The left hot flow heats the front part of the tail boom. The right hot flow is dragged downstream heating this side less as can be observed in Figure 69 and Figure 70.

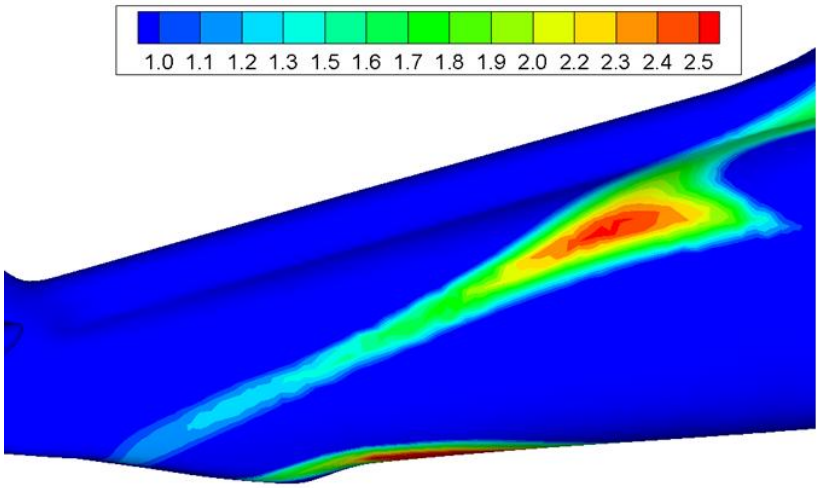

Figure 69 – Temperature distribution on the tail boom at μ=0.07- right side

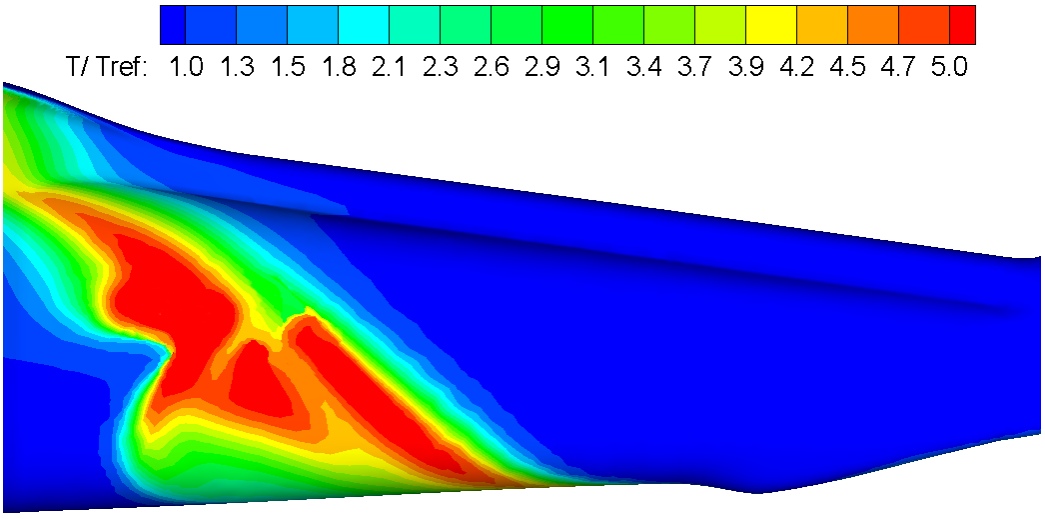

Figure 70 – Temperature distribution on the tail boom at μ=0.28- left side

The right side temperature values at thermocouple positions show similar trends to those of the flight test. According to the numerical results presented in Figure 71 for the upper right side , the downstream of about the x/Lref=0.45 station the hot flow does not affect the tail, although the flight test results show some effect. On the lower right side (Figure 72), the temperature values were underpredicted, particularly on the rear part of the tail boom. The temperature distributions on the left side are highly influenced by the stores (Figure 73-Figure 74). The wake of the stores hit the tail boom as shown in Figure 70 creating a hot spot there.

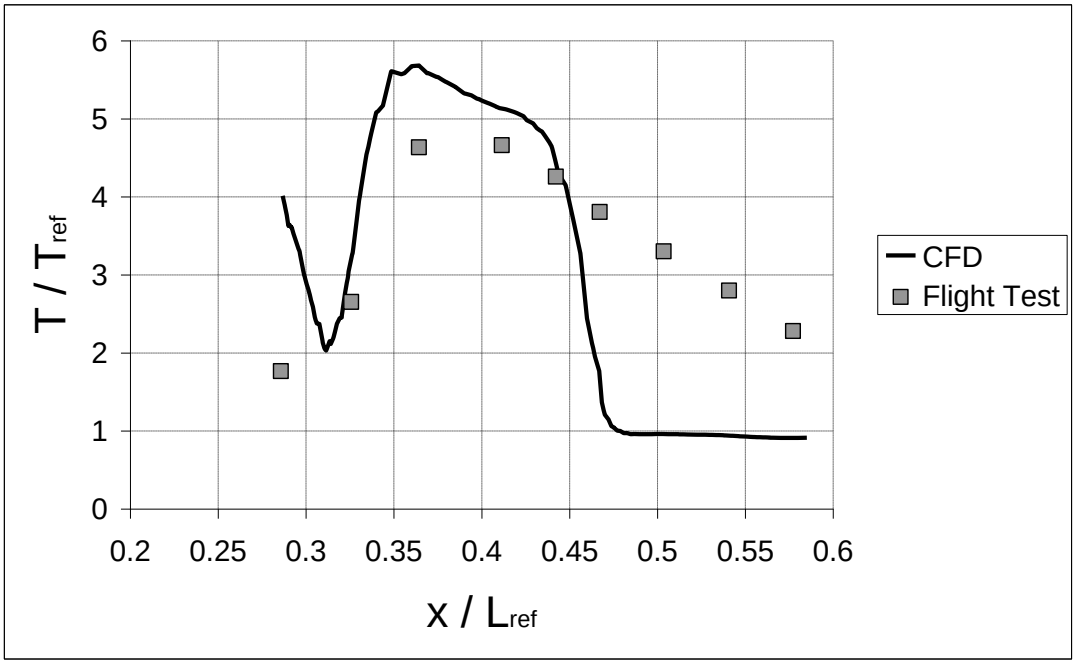

Figure 71 – Temperature values on the upper right data line at μ=0.07

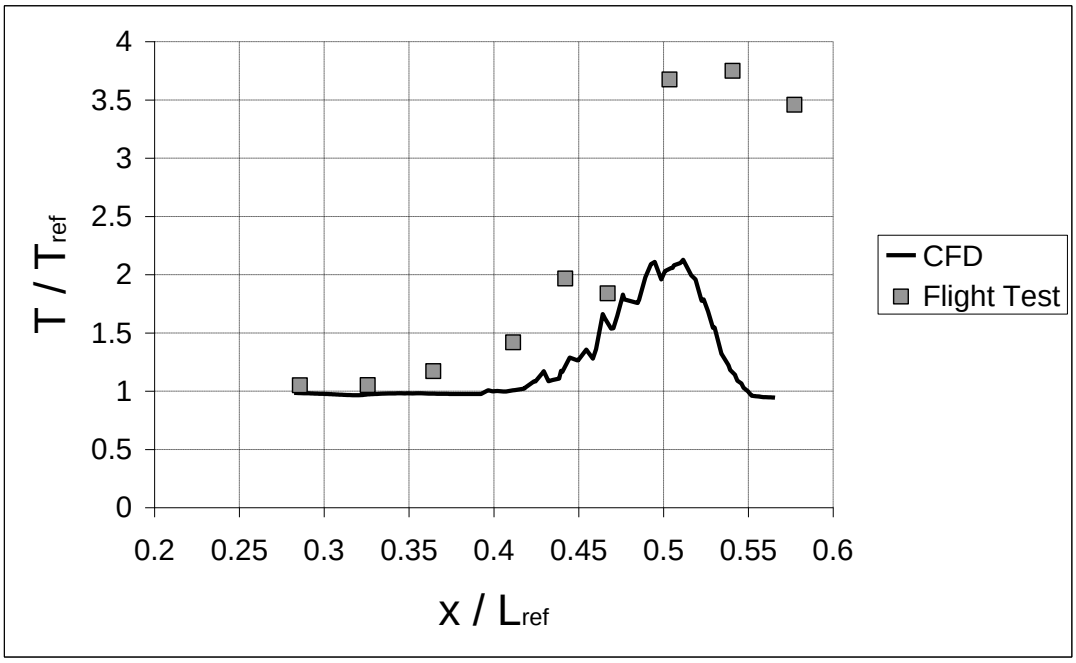

Figure 72 – Temperature values on the lower right data line at μ=0.07

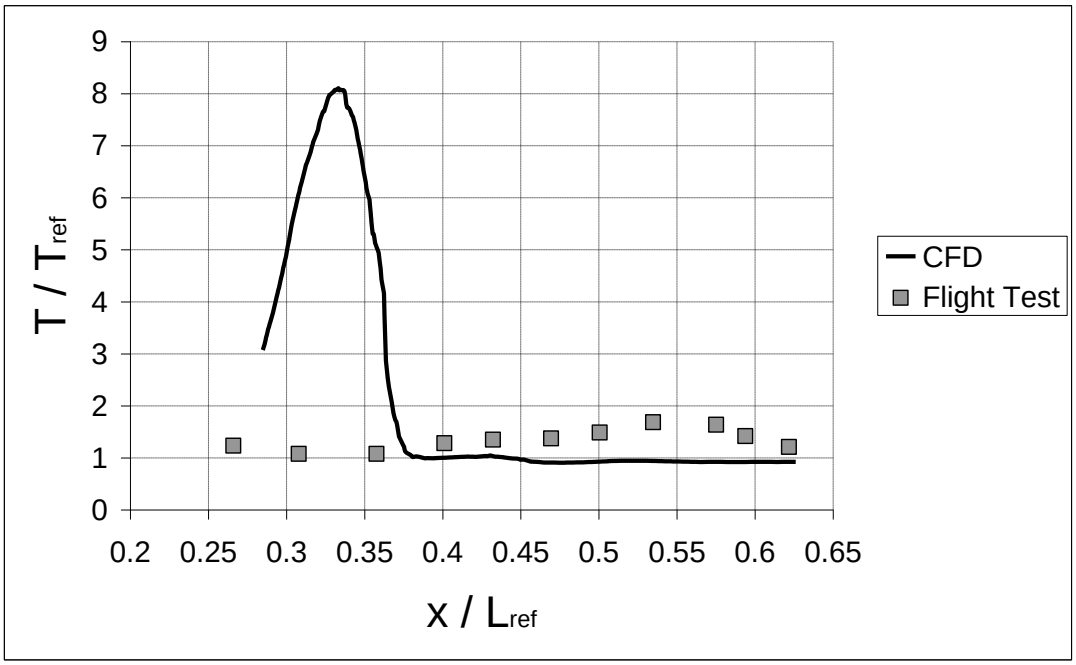

Figure 73 – Temperature values on the upper left data line at μ=0.07

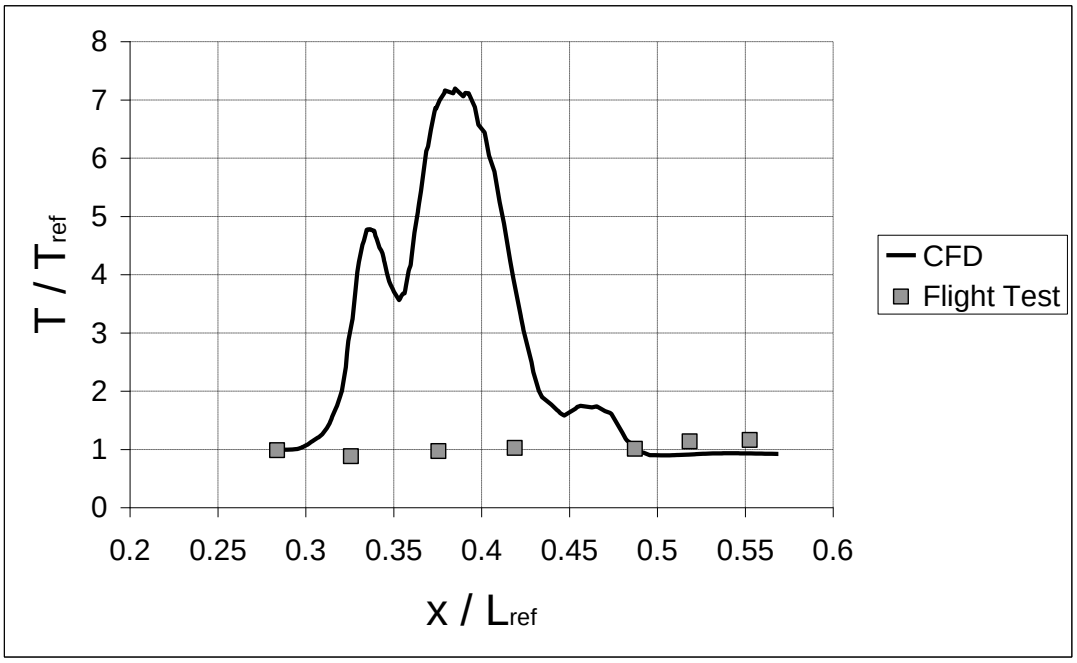

Figure 74 – Temperature values on the lower left data line at μ=0.07

Overall, the results of the μ=0.07 are in less accord with the flight test data. In addition to the causes of discrepancies between the computed results and test data aforementioned in the earlier cases, in the μ=0.07 case there was one more possible source for the differences. The Virtual Blade Model is a time-averaged model. However, with the decreased flight velocity, the increasing influence of the rotor introduces stronger unsteady effects on the tail boom, and the computational approach was a steady one.

4.7 HOVER IN GROUND EFFECT

In the hover in ground effect case, the main rotor wake sheds straight downward over the fuselage and encounters the ground (Figure 75). With the influence of the rotor downwash, the exhaust jet is deflected downwards as soon as it emerges from the nozzle. The rotor downwash directs the exhaust jet as illustrated in Figure 76 and Figure 77.

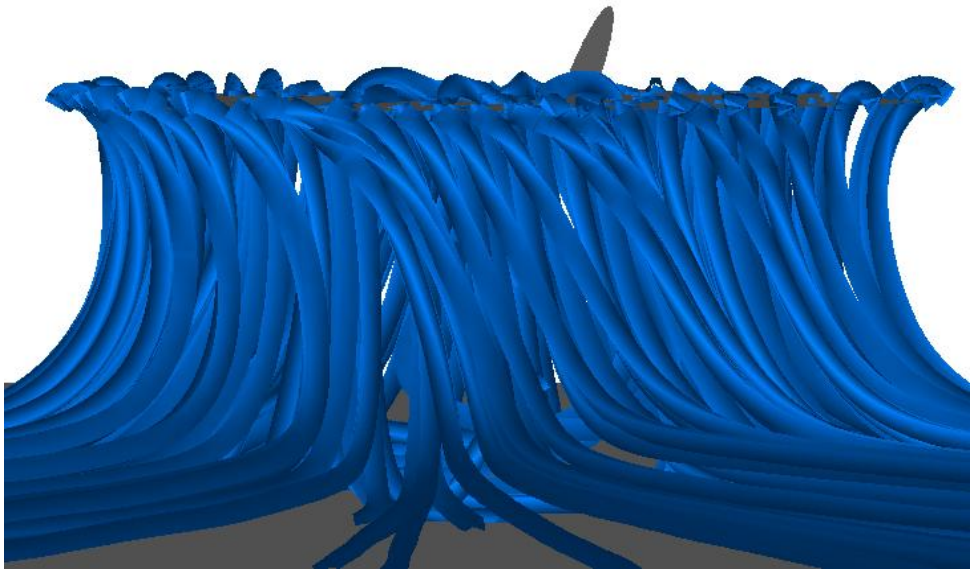

Figure 75 – Main rotor streamlines in hover in ground effect

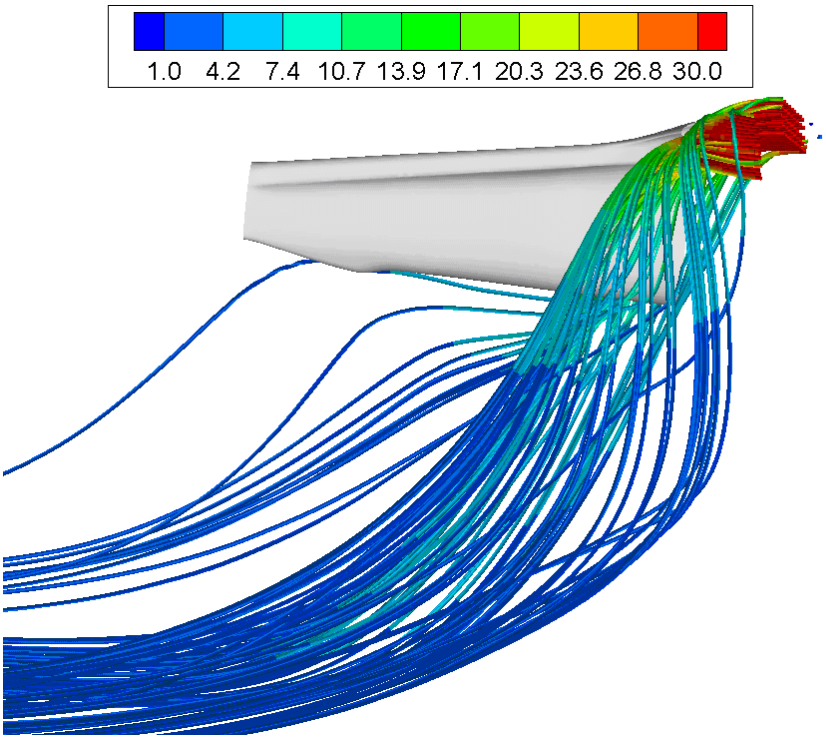

Figure 76 – Exhaust streamlines in hover in ground effect (Colored by T/T_{ref})

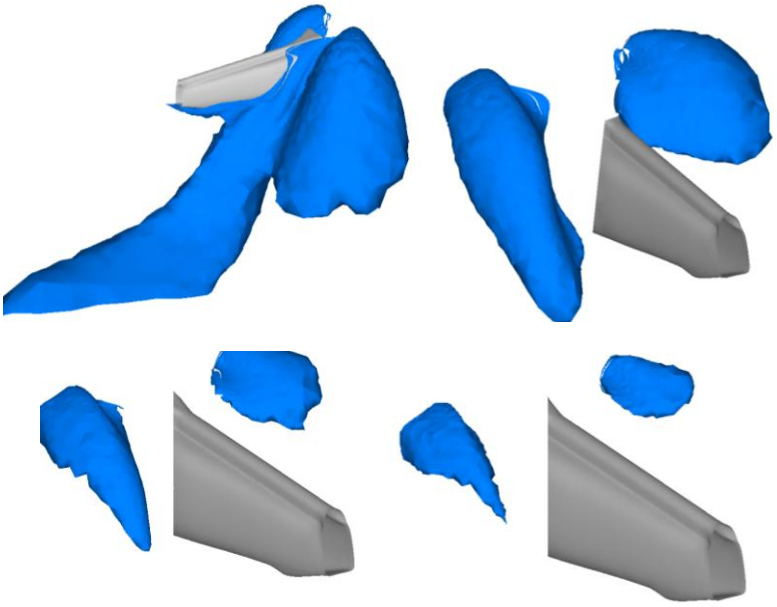

Figure 77 – Temperature isosurfaces in hover in ground effect

When the results shown in Figure 78 and Figure 79 are examined, it is observed that only the front part and the bottom of the tail are heated, since the exhaust jet is deflected downward by the rotor downwash.

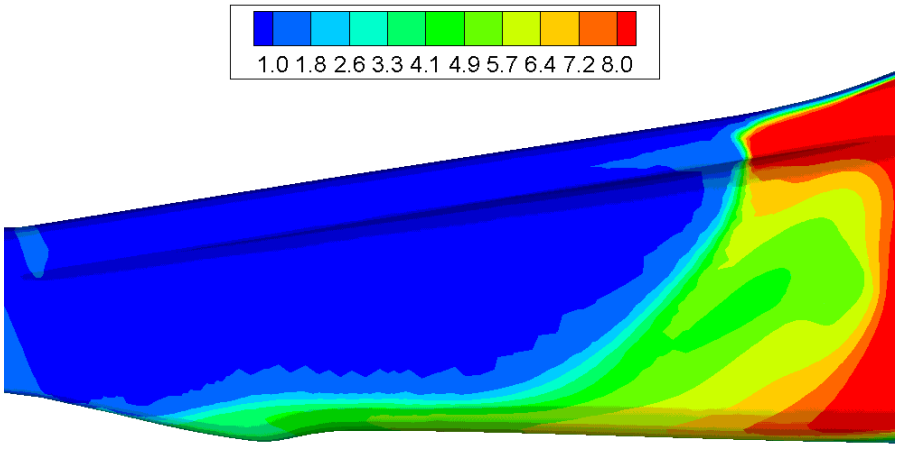

Figure 78 – Temperature distribution on the tail boom in hover in ground effect – right side

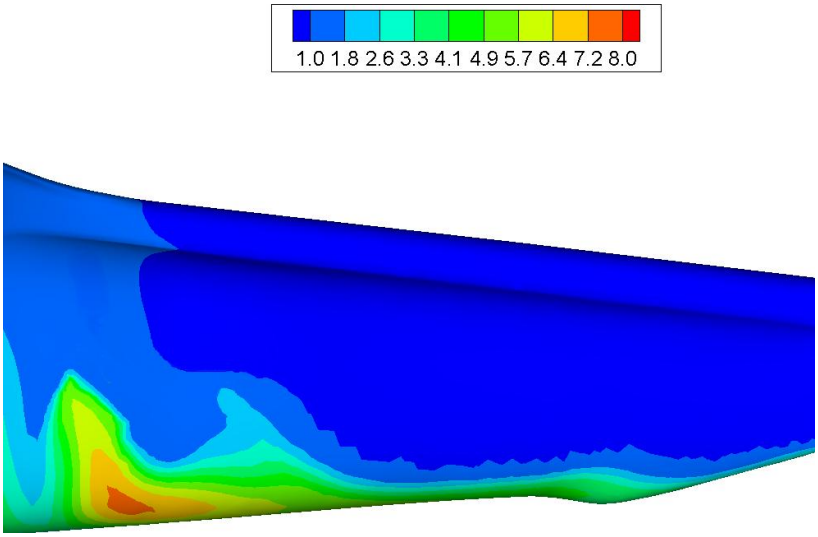

Figure 79 – Temperature distribution on the tail boom in hover in ground effect – left side

The CFD simulation captures the trend in the temperature distribution upstream of x/L_{ref}=0.45 on the upper right side although the values are overpredicted. Downstream of this point, the tail is not under the effect of the exhaust hot flow, and temperature values approach the freestream values. However, the flight test data shows that this region is heated by the hot flow as well (Figure 80). On the lower right side, the numerical analysis correctly predicts the part of the tail that is affected by the hot flow although the values are underpredicted especially downstream of x/L_{ref}=0.47 as can be observed in Figure 81.

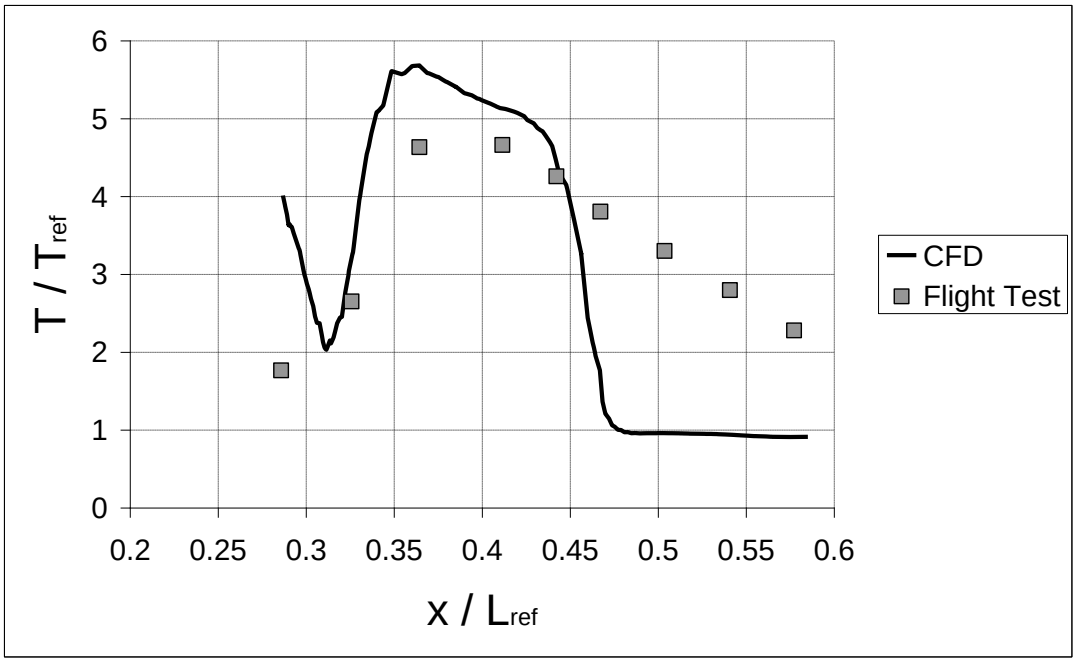

Figure 80 – Temperature values on the upper right data line in hover in ground effect

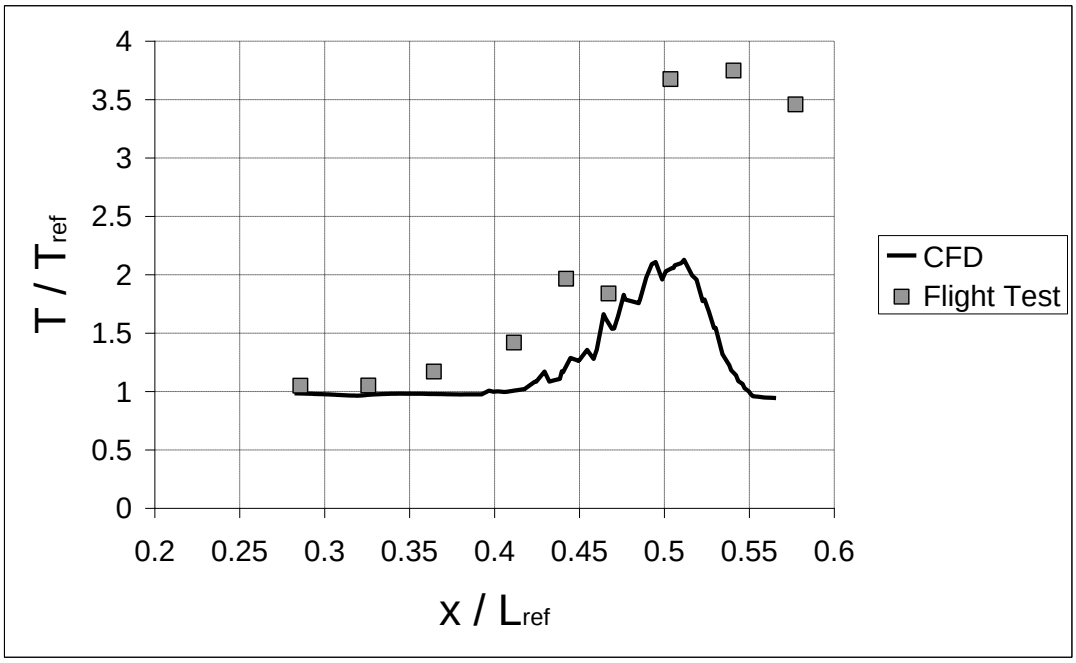

Figure 81 – Temperature values on the lower right data line in hover in ground effect

On the upper and lower left sides heating of the tail boom with the effect of the wakes of the stores is observed (Figure 82 and Figure 83). However, the flight data shows that only downstream of x/L_{ref}=0.45 is heated slightly which is not captured by the CFD analysis. The differences between the numerical results and the flight test data can be attributed to similar factors as in the forward flight cases.

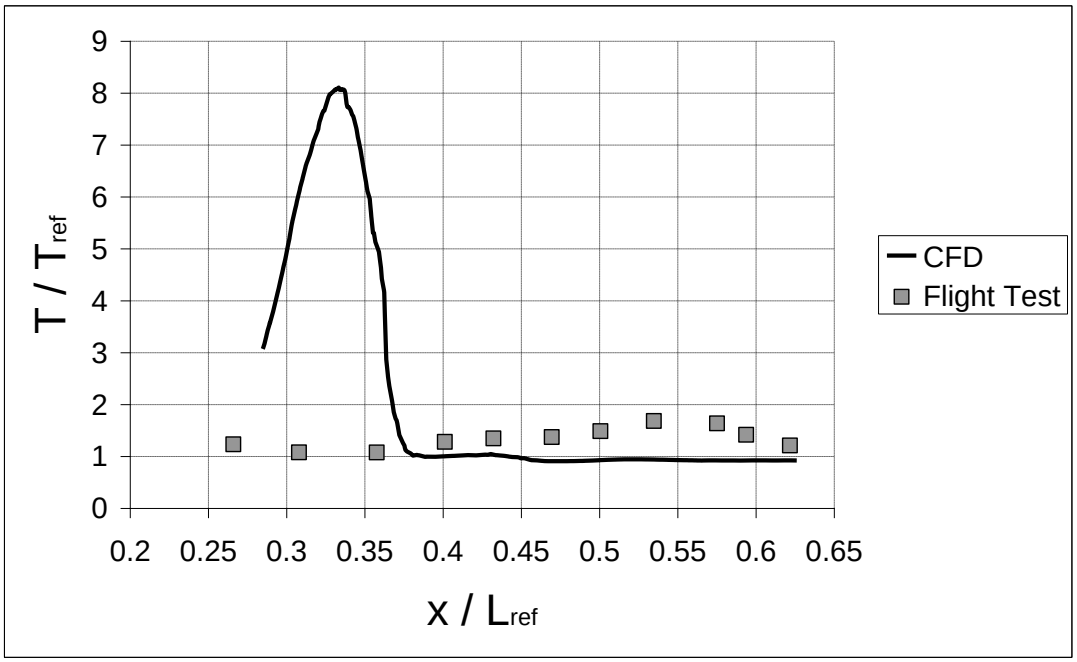

Figure 82 – Temperature values on the upper left data line in hover in ground effect

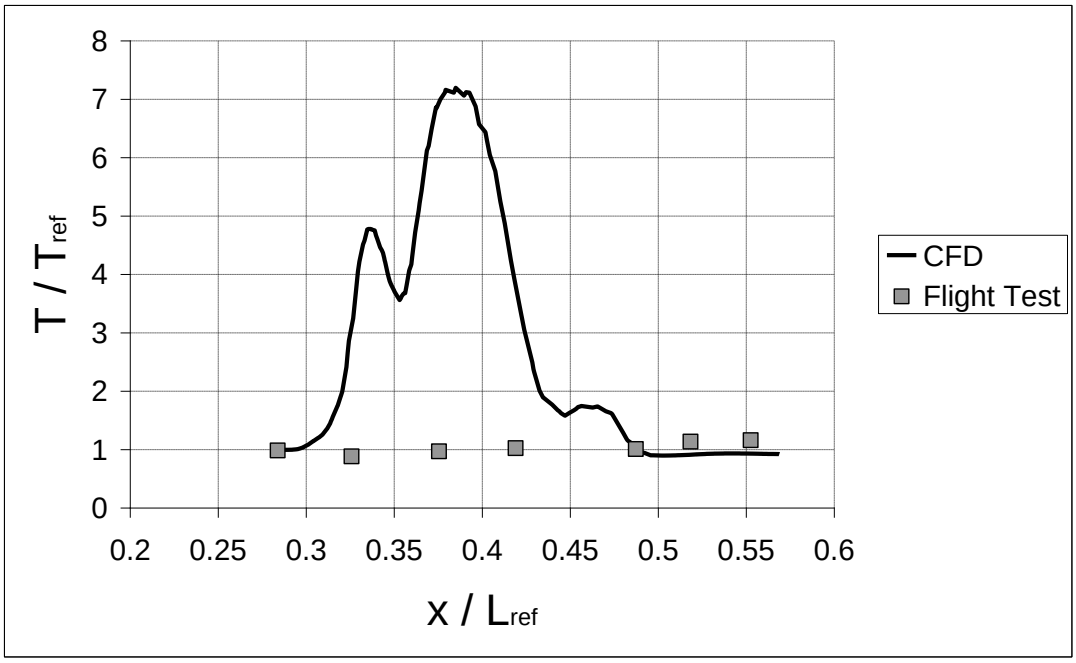

Figure 83 – Temperature values on the lower left data line in hover in ground effect

CHAPTER 5

CONCLUDING REMARKS

In this thesis, helicopter flow fields including thermal effects were investigated. The rotor was accounted for through the use of the Virtual Blade Model, and the engine was included in the simulation via proper inlet and exit boundary conditions. The simulations were performed for four forward flight velocities and hover in ground effect.

Temperature distributions about the tail boom were compared to available flight test data. It was observed that the numerical analyses were successful in capturing the general features of the complex helicopter flow field. The numerical results and the test data showed reasonably good agreement with the test data. However, the temperature values were, in general, overestimated.

The differences between the numerical results and the flight test data can be attributed to the negligence of suppressors, the exhaust temperatures extrapolated from ground tests, negligence of store details, and atmospheric disturbances.

The numerical investigations carried out in this thesis showed that, although need for tests cannot be eliminated totally, CFD can provide important information during design and modification phases. This information can also be used for flight test planning.

REFERENCES

[1] Leishman, J., Principles of Helicopter Aerodynamics, Cambridge University press, 2002

[2] Groninga, K., Mast, T., Goodman, K., Anderson, D., Development and Implementation of the H–1 Turned Exhaust System, American Helicopter Society 61st Annual Forum, Grapevine, TX, 2005

[3] Mineck, R., Application of an Unstructured Grid Navier-Stokes Solver to a Generic Helicopter Body, NASA/TM-1999-209510, 1999

[4] Berry, J., Letnikov V., Bavykina I., Chaffin M., A Comparison of Interactional Aerodynamics Methods For A Helicopter In Low Speed Flight, NASA-TM-1998-208420, 1998

[5] Park, Y., Nam, H., Kwon O., Simulation of Unsteady Rotor-Fuselage Interactions Using Unstructured Adaptive Meshes, American Helicopter Society 59th Annual Forum, Phoenix, Arizona, 2003

[6] O'Brien, D., Analysis of Computational Modeling Techniques for Complete Rotorcraft Configurations, Ph.D. Thesis, Georgia Institute of Technology, May 2006

[7] O'Brien, D., Calvert, M., Butler, S., An Examination of Engine Effects on Helicopter Aeromechanics, AHS Specialist's Conference on Aeromechanics, San Francisco, CA, 2008

[8] Cao Y., Su Y., Zhang Q., Numerical Simulation of Helicopter Engine Jet and Fuselage Temperature Field, Journal of Aircraft Vol.43, No 6, November-December 2006

[9] Dimanlig A., van Dam C, Duque E., Numerical Simulation of Helicopter Engine Plume in Forward Flight, NASA -CR-197488, 1994

[10] Fluent 6.3 Documentation: User's Guide, UDF Manual, Fluent, Inc., 2006

[11]Seddon, J., Newman, S., Basic Helicopter Aerodynamics, AIAA Education Series, 2001

[12] Prouty, R., Helicopter Performance, Stability and Control, Krieger Publishing Company, 1995

[13] GAMBIT 2.3 Documentation: User's Guide, Modeling Guide, Fluent, Inc., 2005

[14] TGrid 5.0 Documentation: User's Guide, ANSYS, Inc., 2008

[15] Ballin M, A High Fidelity Real-Time Simulation of a Small Turboshaft Engine, NASA-TM-100991, 1988

[16] Caliskan S., Development of Forward Flight Trim and Longitudinal Dynamic Stability Codes and Their Application to a UH-60 Helicopter, M.S. Thesis, METU, February 2009

[17] Ruith M, Unstructured, Multiplex Rotor Source Model With Thrust And Moment Trimming - Fluent 's VBM Model, AIAA 2005-5217, 2005

[18] Tecplot User's Manual, Tecplot Inc., 2006